

**Self-imaging and its applications to multimode  
interference (MMI) and photonic bandgap  
devices**

A thesis submitted to  
Nirma University

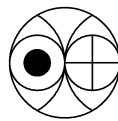


for the degree of  
**Doctor of Philosophy in Physics**

by

**Subimal Deb**

under the Supervision of  
**Prof. Jagannath Banerji**



THEORETICAL PHYSICS DIVISION  
PHYSICAL RESEARCH LABORATORY  
AHMEDABAD - 380009,INDIA

**February, 2009**



*To*  
*my*  
*parents*



---

# Contents

---

List of Figures	v
Acknowledgement	xiii
Abstract	xv
1 Introduction	1
1.1 Self-imaging . . . . .	2
1.1.1 Self-imaging in free space . . . . .	3
1.1.2 Self-imaging in waveguides . . . . .	4
1.2 Conventional MMI devices . . . . .	5
1.3 Photonic band gap structures . . . . .	9
1.3.1 Methods for analysing dielectric structures . . . . .	11
1.3.2 Plane wave expansion . . . . .	12
1.3.3 Order-N method . . . . .	13
1.3.4 Characteristic matrix approach . . . . .	15
1.4 Conclusion . . . . .	19
2 A Dual Case I waveguide resonator with variable reflectivity mirrors	20

2.1	Introduction . . . . .	20
2.2	Theory . . . . .	22
2.2.1	Waveguide Modes . . . . .	22
2.2.2	Self- Imaging and beam splitting . . . . .	24
2.3	Previous design and its working principle . . . . .	26
2.4	Present Design and its working principle . . . . .	27
2.5	Results and Discussion . . . . .	30
2.6	Conclusion . . . . .	36
3	Critical coupling at oblique incidence . . . . .	38
3.1	Introduction . . . . .	38
3.2	Mathematical Formulation . . . . .	41
3.3	Numerical Results and Discussions . . . . .	45
3.4	Conclusions . . . . .	50
4	Photonic crystal waveguide interferometer with $\sim \lambda/1000$ fringe spacing . . . . .	51
4.1	Introduction . . . . .	51
4.2	Previous work . . . . .	52
4.2.1	The experiment of Ovchinnikov and Pfau (year 2001) . . . . .	52
4.2.2	The design of Jenkins et. al. (year 2008) . . . . .	53
4.3	The present design . . . . .	61
4.4	Method used . . . . .	62
4.4.1	Determining the propagation constants . . . . .	63
4.4.2	Extraction of the guided modes . . . . .	65

	iv
4.5 Results . . . . .	67
4.6 Conclusion . . . . .	72
5 Conclusion and future prospects	73
Bibliography	75

---

## List of Figures

---

1.1	<i>Schematic of a planar waveguide. . . . .</i>	6
1.2	<i>Schematic of the conventional waveguide designs. They are characterized by the distance of the mirror from the guide exit (<math>z</math>) and the radius of curvature of the mirror (<math>R</math>).  (a) For the Case I design <math>z = 0</math>, <math>R = \infty</math>.  (b) For the Case II design <math>z \gg z_0</math>, <math>R = z</math>.  (c) For the Case III design <math>z = z_0</math>, <math>R = 2z_0</math>. Here <math>R = z + z_0^2/z</math>, <math>z_0 = \pi w_0^2/\lambda</math> and <math>w_0 = 0.7032a</math>. . . . .</i>	8
1.3	<i>Schematic diagram of one, two and three dimensional photonic crystal structures respectively. . . . .</i>	9
1.4	<i>(Left) Schematic of triangular lattice of circular holes(<math>\epsilon = 1</math>, shown in blue) in a medium with <math>\epsilon = 13</math>(shown in green).  (Right) Photonic band diagram of the structure on the left. The radius of the holes is <math>0.48a</math> where <math>a</math> is the distance between the centres of two nearest holes. . . . .</i>	11
1.5	<i>Schematic of the electric and magnetic field meshes used in the order-<math>N</math> method [1]. . . . .</i>	14

1.6	<i>Line integral of the electric field taken around the magnetic field (penetrating out of the plane of paper) . . . . .</i>	15
1.7	<i>The schematic of the characteristic matrix method. . . . .</i>	16
1.8	<i>The contour plot of reflectivity of 10 pairs of slabs with refractive indices 2.39 and 1.0 bounded on either side by air. The thickness of the individual slabs correspond to <math>\lambda/4</math> plates for normal incidence with <math>\lambda=410\text{nm}</math>. The angle of incidence is in radians. . . . .</i>	18
2.1	<i>Schematic of a self imaging waveguide resonator as reported in an earlier publication [2]. The resonator was formed of a waveguide of square cross section <math>2a \times 2a</math> and of length <math>2a^2/\lambda = L/2</math> , closed at one end (<math>z = 0</math>) by a curved mirror at a distance <math>a^2/2\lambda = L/8</math> from the guide exit, and bounded at the other end (<math>z = L/2</math>), by a plane mirror. . . . .</i>	25
2.2	<i>A new design for self-imaging waveguide resonators in which the end-mirrors are plane with step-reflectance profiles. We assume that the reflectivity of the mirror <math>M_1</math> at the (<math>z = 0</math>) plane is <math>r_1</math> on a square block (<math>2b \times 2b</math>) centered at the origin and <math>r_2</math> elsewhere with <math>r_1 \approx 1</math> and <math>r_2 \approx 0</math>. The reflectivity of the mirror <math>M_2</math> at the (<math>z = L/2</math>) plane, on the other hand, is taken to be <math>r_2</math> on a square block (<math>2c \times 2c</math>) centered at the origin and <math>r_1</math> elsewhere. . . . .</i>	27

- 2.3 *Round-trip fractional loss of the first six resonator modes (all of which are symmetric solutions) in the  $x$ - $z$  plane as a function of  $b/a$  when  $c = 0$ . The thick red line corresponds to the lowest-loss mode. All the calculations have been carried out in Mathematica 6.0. . . . . 31*
- 2.4 *Profiles for the two lowest loss resonator modes in the  $x$ - $z$  plane at (a)  $z = 0$  and at (b)  $z = L/2$  when  $b/a = 0.44$  and  $c = 0$ . The dotted line corresponds to the lowest loss mode whereas the solid line corresponds to the other mode. . . . . 32*
- 2.5 *Round-trip fractional loss for the first six resonator modes (in ascending order of fractional loss) in the  $x$ - $z$  plane, as a function of  $c/a$  when  $b/a = 0.44$ . The thick red line corresponds to the lowest-loss mode. . . . . 33*
- 2.6 *Round-trip fractional loss for the first six resonator modes in the  $x$ - $z$  plane as a function of the resonator length when  $b/a = c/a = 0.44$ . The thick red line corresponds to the lowest-loss mode. . . . . 34*

- 2.7 *The transverse intensity profiles in the  $x$ - $z$  plane, at each end of the resonator and inside the waveguide for the two lowest loss resonator modes when  $b/a = c/a = 0.44$  and the resonator length is set at  $L/2 = 2a^2/\lambda$ . The left column represents the profiles for the lowest-loss mode in the  $+z$  direction, and the right column represents the profiles for the next mode (in ascending order of fractional loss). In each column, the bottom figure displays the intensity profile at  $z = 0$ , the middle figure is the contour plot of the intensity profile inside the waveguide, and the top figure is the intensity profile at  $z = L/2$ . . . . . 35*
- 2.8 *The mirror reflectivity is set at 0.9 for the high-reflectivity segments and at 0.1 for the low reflectivity segments. (a) Round-trip fractional loss for the first six resonator modes in the  $x$ - $z$  plane as a function of the resonator length. All other details are as in Fig. 2.6. (b) Intensity profiles for the lowest-loss mode at  $z = 0$  (bottom figure) and  $z = L/2$  (top figure). (c) The same as in (b) for the next mode (in ascending order of fractional loss). . . . . 36*
- 3.1 *Schematic diagram of the layered medium. . . . . 39*
- 3.2 *Real and Imaginary parts of the complex dielectric function for the composite material. Curves from top to bottom are for  $f = 0.1, 0.05$  and  $0.01$  respectively. The dashed curve corresponds to bulk metal ( $f = 1.0$ ). . . . . 43*

- 3.3 Total scattering  $R + T$  (solid lines) as functions of wavelength  $\lambda$  for (a) TE and (b) TM polarization for  $d_1 = 10$  nm,  $d_2 = 75$  nm and  $f = 0.05$ . Curves marked by 1, 2 and 3 correspond to  $\theta = 0^\circ$ ,  $45^\circ$  and  $60^\circ$ , respectively. The inset shows a magnification near  $R + T = 0$ . Other parameters are  $N = 10$ ,  $\epsilon_i = 1.0$ ,  $\epsilon_h = 2.25$ ,  $\epsilon_f = 2.25$ ,  $\epsilon_a = 5.7121$ ,  $\epsilon_b = 2.6244$ . The normal incidence transmission and reflection for the total structure are also shown by dashed and dotted lines, respectively. . . . . 46
- 3.4 Oblique incidence (at  $\theta = 45^\circ$ ) transmission (dashed line) and reflection (solid line) of the bare composite film with  $f = 0.05$ ,  $d_1 = 10$  nm on the substrate for (a) TE and (b) TM polarizations. The transmission for  $f = 1.0$  (dotted line) is shown for reference on both the panels. Oblique incidence (at  $\theta = 45^\circ$ ) total scattering  $R + T$  (solid lines) as functions of  $\lambda$  for  $d_1 = 10$  nm,  $f = 0.05$ , for (c) TE polarization with  $d_2 = 30$ , 45 and 65 nm (curves 1, 2 and 3, respectively) and for (d) TM polarization with  $d_2 = 30$ , 51 and 65 nm (curves 1, 2 and 3, respectively). The inset in 4(d) shows a magnification near  $R + T = 0$ . Other parameters are as in Figure 3.3. . . . . 47

3.5	<i>Oblique incidence (at <math>\theta = 45^\circ</math>) intensity reflection as a function of <math>\lambda</math> for a 70 nm thick composite film on a substrate ((a) and (b)) and for the total structure ((c) with <math>d_2=85</math> nm and (d) with <math>d_2=98</math> nm). The left panels ((a) and (c)) are for TE incidence, while the right ones ((b) and (d)) are for TM. Curves 1, 2 and 3 in the left panels correspond to <math>f=0.01</math>, 0.05 and 0.1, respectively, while those on the right correspond to <math>f=0.01</math>, 0.03 and 0.06, respectively. The transmission (dotted line) is shown for reference with <math>f = 0.1</math> for TE and with <math>f = 0.06</math> for TM polarization. Other parameters are as in Figure 3.3 . . . . .</i>	48
4.1	<i>Schematic diagram of the fiber coupled waveguide interferometer in [3] . . . . .</i>	52
4.2	<i>Schematic diagram of the fiber coupled waveguide interferometer in [4] . . . . .</i>	54
4.3	<i>Excitation of guided modes as a function of the input angle of the injected beam[4] . . . . .</i>	56
4.4	<i>The power coupling coefficient plots of a <math>8\mu\text{m}</math> wide waveguide with gold mirror walls at (top) the input plane (<math>z=0</math>) and (bottom) the output plane (<math>z=5\text{cm}</math>). Only insignificant amounts of the <math>TE_3</math> and <math>TE_4</math> modes survive at the guide exit. .</i>	59

4.5	<i>The change in guide width required to produce a complete switching cycle of the beam at the output plane[4]. This plot is for <math>L = 5\text{cm}</math> and <math>\lambda = 1.32\mu\text{m}</math>.</i>	60
4.6	<i>The power coupling coefficient plots of a <math>4\mu\text{m}</math> wide waveguide with gold mirror walls at (top) the input plane (<math>z=0</math>) and (bottom) the output plane (<math>z=5\text{cm}</math>)</i>	61
4.7	<i>Transformation of coordinates for the tilted beam injected into the waveguide.</i>	66
4.8	<i>Attenuation constants corresponding to the first two modes using analytical formula (solid lines) and the finite difference scheme (dots) for the system in [4].</i>	67
4.9	<i>The power coupling coefficient plots of a <math>11\mu\text{m}</math> wide waveguide with gold mirror walls at (top) the input plane (<math>z=0</math>) and (bottom) the output plane (<math>z=5\text{cm}</math>)</i>	68
4.10	<i>Plot of the power coupling coefficient vs input angle of the beam for various thickness of the finite photonic crystal walls at a guide width of <math>4\mu\text{m}</math>. The left column is the profile at the input plane(<math>z=0</math>). The plots on the right side are the power coupling coefficients at the exit plane(<math>z=5\text{cm}</math>). The cladding beyond the photonic crystal layers are of absorbing material (Ge). There is a slight attenuation with 7 pairs of slabs (a). There is no change of the power coupling coefficient profile if 10 or more layers( (b) and (c) respectively) are used.</i>	69

- 4.11 *The contour plots of the electric field intensities at the exit plane for different guide widths. The values of the guide widths are given above the figures. . . . . 70*
- 4.12 *The power coupling coefficient plots of a 4m wide waveguide with photonic crystal walls at (left) the input plane ( $z=0$ ) and (right) the output plane ( $z=5\text{cm}$ ) . . . . . 71*

---

## Acknowledgement

---

The completion of this thesis involves the help and support of many people. I express my sincere gratitude to all of them - without their help this work wouldn't plausibly have attained its current form.

I am indebted to my supervisor, Prof. J. Banerji, for his patience and efforts to educate me with the basics and tools necessary for the work in this volume.

Prof. Subhasish Dutta Gupta has been an inspiration to me and I thank him for giving me the opportunity to work with him. I am grateful to Dr. R. P. Singh and Prof. P. K. Panigrahi for their constant encouragement and support.

I had plenty of academic discussions with Tarakda during and after his tenure in PRL. He gave me a kick-start with the Linux operating system that helped me carry out most of my calculations. Subhasis (Subhasis Mahapatra) eased my computational difficulties and helped me become comfortable with the Linux OS. Without Subhasis around, the pace of my progress would have surely been impeded. Regardless of my efforts to put them down here, my gratitude to Tarakda and Subhasis shall remain unexpressed in entirety. I

thank all my friends and colleagues especially Shreyas, Parimal, Amit, Sanat, Uma, Satya, Ayan, Priyam, Rajneesh, Charan, Arpitadi, Jhuma, Anirban, Soumen, Utpalda and Suranjanadi for being patient audience.

I thank all the members of our library and computer centre for their prompt help and support.

My parents receive my deepest gratitude for their boundless love, support and sacrifice. I dedicate this thesis to them.

Subimal Deb

---

## Abstract

---

An introduction to the self-imaging phenomenon, an overview of conventional multimode interference devices and photonic band gap materials is provided in Chapter 1. In Chapter 2 a novel class of a waveguide resonator based on self-imaging has been proposed. It is an improvement on a previous self-imaging based design. A critically coupled resonator is analyzed for oblique incidence in Chapter 3. An ultra sensitive waveguide interferometer having a fringe spacing of  $\sim \lambda/1000$  is described and analyzed in Chapter 4.

---

# 1 Introduction

---

The repetition of an electromagnetic field pattern along the direction of propagation, or self-imaging, was discovered by Henry Fox Talbot and explained later by Lord Rayleigh. Self-imaging can occur both in free space (known as Talbot Effect, for a periodic input field) and inside multimode rectangular cross sectioned waveguides. Multimode interference (MMI) devices are based on the principle of self-imaging and have numerous applications in telecommunications since they are compact, have a low loss, a high optical bandwidth and a high fabrication tolerance. They are widely used in planar waveguide devices. In the paraxial approximation, a symmetric electromagnetic field profile propagating in a rectangular waveguide repeats itself at distances of  $L = 4b^2/\lambda$  where  $b$  is the guide half-width and  $\lambda$  is the wavelength of the propagating field. Anti-symmetric beams and beams with no definite parity repeat at intervals of  $2L$  and  $8L$  respectively in rectangular multimode waveguides.

Photonic crystals or photonic band gap materials are periodic dielectric structures that can inhibit the propagation of electromagnetic waves through them. One-dimensional structures were known for a long time and have

seen applications like the dielectric Bragg reflector. Higher dimensional periodic structures have been studied since 1987 following the proposals by Sajeev John for light localization and Yablonovitch for guiding electromagnetic waves. Photonic crystals are being tailored along similar lines as semiconductor devices (considering their strong analogy) for providing good guiding structures for electromagnetic radiation. The inhibition of propagation takes place due to Bragg scattering off the interfaces in the dielectric structure [5, 6, 7, 8].

In this chapter an overview of self-imaging, multimode interference devices, photonic crystals and few of the methods used for their analysis will be presented.

## 1.1 Self-imaging

Self-imaging, the phenomenon of reproduction of a wavefield at regular intervals along the direction of propagation, was discovered more than 170 years ago by Henry Fox Talbot in 1836[9] and explained analytically by Lord Rayleigh in 1881. For a linear grating illuminated by light of wavelength  $\lambda$  and having a plane wavefront, he showed that the intensity distribution repeats itself at distances of  $2d^2/\lambda$  along the direction of propagation of the wave, where  $d$  is the grating period.

Subsequent related studies (see for example [10]) were on grating image formation ion microscopy, Fresnel diffraction field behind periodic objects and the general conditions that an object must satisfy for repetition of its

complex amplitude transmittance along the illumination direction. Periodic structures exist in other fields of science such as crystallographic structures and hence self-imaging has been studied in various fields like optics, electron-microscopy and acousto-optics. In the field of optics, there have been applications in image processing and synthesis, production of optical elements, optical testing and optical metrology. This phenomenon is still actively studied by many researchers from the scientific as well as the technological perspective.

### 1.1.1 Self-imaging in free space

A periodic object (for example, a uniformly illuminated grating) is the simplest example for the demonstration of the Talbot effect. If the grating is periodic along the x-axis and the illuminating monochromatic beam propagates along the z-axis, the complex amplitude just behind the grating is

$$u(x, 0) = \sum_m c_m \exp(2\pi imx/L) \quad (1.1)$$

The amplitude of the propagating wave at a different plane (in the paraxial approximation) is given by

$$u(x, z) \propto \int_{-\infty}^{\infty} \exp\left(ik \frac{(x - x_0)^2}{2z}\right) \sum_m c_m \exp\left(i \frac{2\pi mx_0}{L}\right) dx_0 \quad (1.2)$$

This finally gives

$$u(x, z) \propto \sum_m c_m \exp\left(i\frac{2\pi m x_0}{L}\right) \exp\left(-i\frac{\pi m^2 \lambda z}{L^2}\right) \quad (1.3)$$

This shows that for an illuminated object of periodicity  $L$ , its image repeats at distances of  $z_T = 2L^2/\lambda$ . This is called the Talbot effect and  $z_T$  is called the Talbot distance.

### 1.1.2 Self-imaging in waveguides

Self-imaging can also occur in waveguides [11]. The guided modes that are excited in a waveguide interfere while propagating along the waveguide channel. The phases picked up by the various modes are different and at a certain distance beyond the input plane, where the phase differences between the modes equals an integer multiple of  $2\pi$ , the input profile is regenerated. Expressed mathematically, the field at the input plane ( $z = 0$ ) in the waveguide can be written down as a superposition of the guided mode profiles  $F_m(x)$  with coefficients  $a_m$

$$u(x, 0) = \sum_m a_m F_m(x) \quad (1.4)$$

where  $m$  corresponds to the mode index. At a distance  $z$  from the input plane, the modified field is written as

$$u(x, z) = \sum_m a_m F_m(x) \exp(i\beta_m z) \quad (1.5)$$

where  $\beta_m$  is the propagation constant corresponding to the  $m$ -th guided mode. For example, in planar waveguides of width  $2a$  with metallic walls the propagation constants are given by [4]

$$\beta_m = \frac{2\pi}{\lambda} \left[ 1 - \left( \frac{m\lambda}{4a} \right)^2 \right]^{1/2} \quad (1.6)$$

where  $\lambda$  is the wavelength and  $m$  is the mode index. In the paraxial approximation,

$$\beta_m \approx \frac{2\pi}{\lambda} \left[ 1 - \frac{1}{2} \left( \frac{m\lambda}{4a} \right)^2 \right] \quad (1.7)$$

This implies

$$(\beta_m - \beta_p)z = \frac{2\pi}{\lambda} \frac{1}{2} \left( \frac{\lambda}{4a} \right)^2 (p^2 - m^2)z \quad (1.8)$$

would equal an integer multiple of  $2\pi$  at distances of  $16a^2/\lambda$  when all the modes are excited.

## 1.2 Conventional MMI devices

Any structure capable of guiding light from one place to another is an optical waveguide. The simplest and most well known optical waveguide is an optical fiber. The mechanism of guidance of light through an optical fiber is total internal reflection. Solutions of the electromagnetic wave equation for the system are called the modes of the system. These field profiles propagate unchanged through the system and are characterized by their propagation constants. For example, a planar waveguide with the axis along the  $z$ -

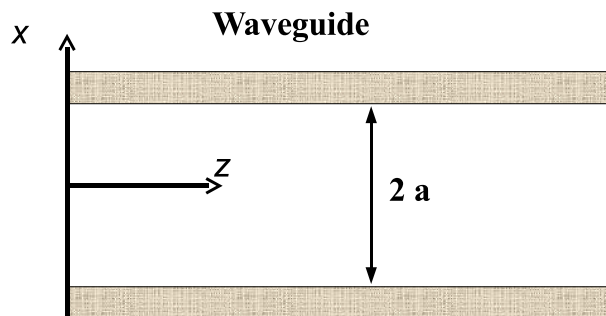


Figure 1.1: *Schematic of a planar waveguide.*

direction, and the x-axis being along the transverse direction, the scalar wave equation

$$\frac{d^2 E(x)}{dx^2} + k_0^2 \epsilon(x) E(x) = \beta^2 E(x) \quad (1.9)$$

has a solution of the form

$$E(x, z) = \sum_m E_m(x) \exp(-i\beta_m z) \quad (1.10)$$

where  $E_m(x)$  is the transverse mode profile of the m-th mode having a propagation constant  $\beta_m$ . If a waveguide admits more than one mode profile as solutions to the wave equation, it is called a multimode waveguide. Propagation along the waveguide channel proceeds with the interference of the modes in a multimode waveguide. Devices using this mechanism of interference of modes are called multimode interference (MMI) devices. Examples of such devices are directional couplers, self imaging waveguides, etc.

The modes of a planar waveguide of width  $2a$  (Figure 1.1) are given by

$$E_m(x, a) = \frac{1}{\sqrt{a}} \begin{cases} \cos(\pi mx/2a) & , \text{ if } m \text{ is odd;} \\ \sin(\pi mx/2a) & , \text{ if } m \text{ is even.} \end{cases} \quad (1.11)$$

These modes satisfy the orthogonality relation

$$\int_{-a}^a E_m(x, a) E_n(x, a) dx = \delta_{mn} \quad (1.12)$$

The corresponding propagation constant is given by  $\beta_m = \frac{2\pi}{\lambda} \left(1 - \frac{1}{2} \left(\frac{m\lambda}{4a}\right)^2\right)$

There are three known waveguide resonator designs[12]. In the Case I design a plane mirror is placed at the guide exit. In the Case II and Case III designs curved mirrors with radius of curvature  $z$  and  $2z_0$  and guide exit to mirror distance much larger than  $z_0$  and equal to  $z_0$  respectively are used. Here the radius of curvature of the wavefront is  $R = z + z_0^2/z$ , the Rayleigh range is  $z_0 = \pi w_0^2/\lambda$  and the beam waist is  $w_0 = 0.7032a$ . The mirror curvature is phase matched with the beam wavefront so that the lowest loss mode is efficiently coupled back into the waveguide. The beam waist is chosen so that the lowest loss mode of the resonator gives the closest match with a Gaussian output. Waveguide resonators have been designed using these configurations but only recently self-imaging has been taken into account in [2]. In this relatively new self-imaging based design, a plane mirror at one end and a curved mirror (phase-matched with the lowest loss mode, distant  $a^2/2\lambda$  from the guide exit) at the other were used. It was shown to effectively

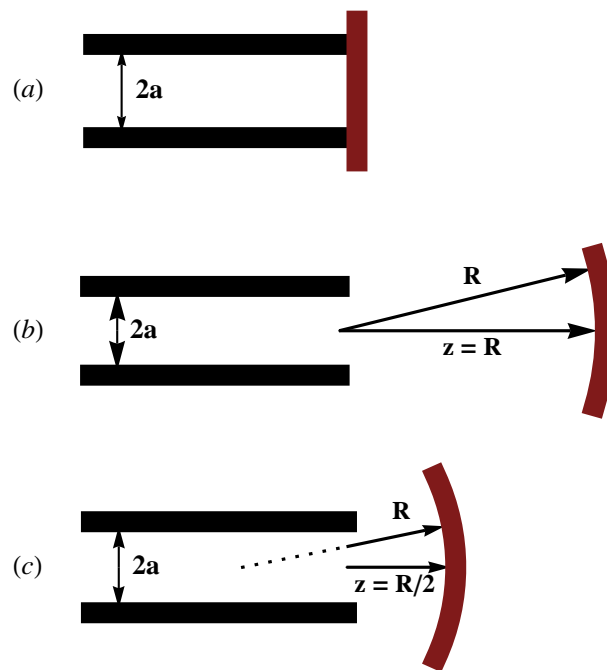


Figure 1.2: *Schematic of the conventional waveguide designs. They are characterized by the distance of the mirror from the guide exit ( $z$ ) and the radius of curvature of the mirror ( $R$ ).*

(a) *For the Case I design  $z = 0$ ,  $R = \infty$ .*

(b) *For the Case II design  $z \gg z_0$ ,  $R = z$ .*

(c) *For the Case III design  $z = z_0$ ,  $R = 2z_0$ . Here  $R = z + z_0^2/z$ ,  $z_0 = \pi w_0^2/\lambda$  and  $w_0 = 0.7032a$ .*

remove the higher order modes and produce a  $\text{TEM}_{00}$  output. In Chapter 2 an improvement on the design of [2] is presented using self imaging and Case I mirrors with variable reflectivity profiles at both ends.

### 1.3 Photonic band gap structures

Photonic band gap structures, as rightly suggested by the name, are dielectric structures that prohibit the propagation of light of certain frequency bands. The one dimensional multilayer structures were studied more than a hundred years by Lord Rayleigh[13] before the higher dimensional counterparts were proposed in 1987[14, 15] by Eli Yablonovitch and Sajeev John. They are also called photonic crystal structures owing to their strong analogy to semiconductor lattice systems (also see [16]).

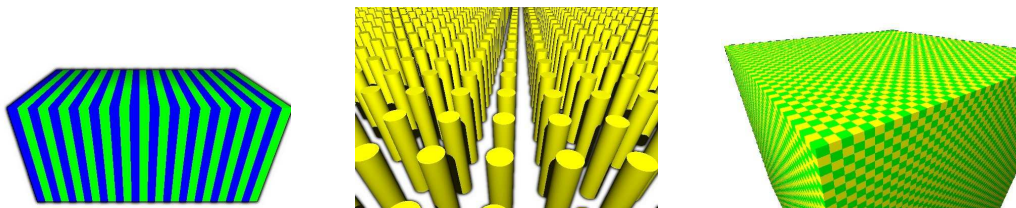


Figure 1.3: *Schematic diagram of one, two and three dimensional photonic crystal structures respectively.*

A schematic diagram of the photonic crystal structures are shown in Figure 1.3. A one dimensional structure may be composed of slabs of two materials placed alternately (as in the figure) or may be a repetition of a stack of more materials. The two dimensional structures are a regular array of rods arranged in a square lattice (see figure) or in some other pattern,

for example, a triangular lattice. The rods may themselves have different cross-sections - circular, square, etc. and similarly, for the three dimensional systems.

The one dimensional structures were known to act as filters for certain frequency bands. The central frequency and the width of the band are determined by the average dielectric constant and the dielectric contrast of the materials of the band. The prohibition of propagation takes place along the direction perpendicular to the stacks. The two and three dimensional photonic crystal structures are capable of preventing electromagnetic wave propagation along two and three directions (along the lattice translation vectors) respectively.

The dielectric distribution in any photonic crystal structure is given as

$$\epsilon(\vec{r}) = \epsilon(\vec{r} + \vec{T}) \quad (1.13)$$

where  $\vec{T} = \sum_{i=1}^N n_i \vec{a}_i$  is a lattice translational vector,  $\vec{a}_i$  are the primitive lattice vectors,  $n_i$  are integers and  $N = 1, 2, 3$  for one, two and three dimensional (respectively) photonic crystal structures. From the two curl equations of Maxwell, one obtains the following equation for the magnetic field  $\vec{H}$

$$\nabla \times \left( \frac{1}{\epsilon(\vec{r})} \nabla \times \vec{H} \right) = \left( \frac{\omega}{c} \right)^2 \vec{H} \quad (1.14)$$

The operator  $\nabla \times \left( \frac{1}{\epsilon(\vec{r})} \nabla \times \right)$  is Hermitian and positive-definite for real  $\epsilon > 0$ . Consequently the eigenfrequencies are real. The mathematical

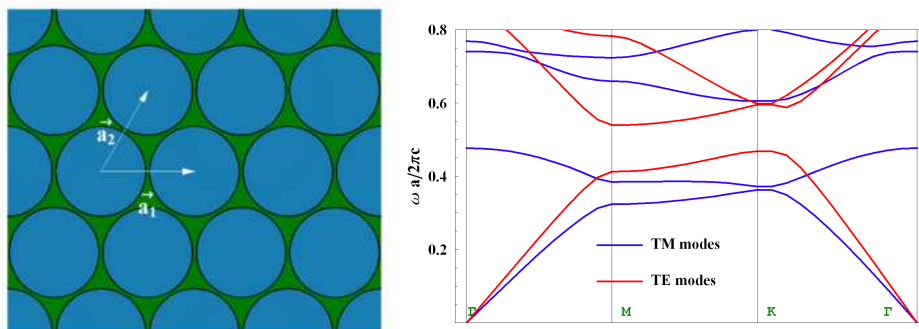


Figure 1.4: (Left) Schematic of triangular lattice of circular holes( $\epsilon = 1$ , shown in blue) in a medium with  $\epsilon = 13$ (shown in green). (Right) Photonic band diagram of the structure on the left. The radius of the holes is  $0.48a$  where  $a$  is the distance between the centres of two nearest holes.

treatment for photonic crystal structures so far follows that of quantum mechanical problems. In addition, the electromagnetic problem in these periodic structures have the transversality condition  $\nabla \cdot \vec{H} = 0$  and  $\nabla \cdot \epsilon \vec{E} = 0$ . The dispersion diagram of the photonic crystal structure is a plot of  $\omega(\vec{k})$  and forms discrete bands(for example see Figure 1.4). There are ranges of frequencies for which the above equation does not admit any solution corresponding to the photonic band gap. The transverse electric (red curves in Figure 1.4) and transverse magnetic (blue curves in Figure 1.4) polarizations show different dispersions. The structure is said to have a complete band gap when the forbidden bands of both the polarizations overlap.

### 1.3.1 Methods for analysing dielectric structures

Since the discovery of the two and three dimensional structures, there have been extensive studies of these systems. Numerous techniques such as the

plane wave expansion method[17, 18], the transfer matrix method[19, 20], the method of multipole moments[21], the Green's function approach[22], the finite difference time domain method[23], the finite element method, etc.(for example [24, 25, 26, 27]) were developed and used [28, 29, 30, 31, 32, 33, 34, 35] for their analysis. Of these, the plane wave expansion method was the one to be used extensively for studying the dispersion characteristics. Each of these methods have their advantages and disadvantages and are used as per the problem at hand. Below we summarize the plane wave expansion technique, the transfer matrix method and the characteristic matrix approach.

### 1.3.2 Plane wave expansion

The plane wave expansion method [17, 18, 36, 37] has been the most popular tool for the analysis of periodic dielectric structures(for example [38, 39, 40, 41, 42]). In this technique, the master equation (Equation 1.14) is rewritten in Fourier space to form an algebraic eigenvalue equation. The eigenvalues are then solved for to find the dispersion of the photonic crystal structure. For periodic dielectric structures one applies the Bloch-Floquet theorem, choosing the eigenfunction as a superposition of the form

$$\vec{H}(\vec{r}) = \sum_{\vec{G}} \sum_{\lambda=1}^2 h_{\vec{G},\lambda} \hat{e}_\lambda \exp(i(\vec{k} + \vec{G}) \cdot \vec{r}) \quad (1.15)$$

Here  $\vec{k}$  is a wave vector and  $\vec{G}$  is a reciprocal lattice vector. For each  $\vec{G}$  there are two polarization vectors  $\hat{e}_1$  and  $\hat{e}_2$  so that

$$\hat{e}_\lambda \cdot (\vec{k} + \vec{G}) = 0, \lambda = 1, 2 \quad (1.16)$$

This gives

$$\sum_{\vec{G}', \lambda'} H_{\vec{G}, \vec{G}'}^{\lambda, \lambda'} h_{\vec{G}', \lambda'} = \frac{\omega^2}{c^2} h_{\vec{G}, \lambda} \quad (1.17)$$

where

$$H_{\vec{G}, \vec{G}'} = |\vec{k} + \vec{G}| |\vec{k} + \vec{G}'| F\left(\frac{1}{\epsilon(\vec{G} - \vec{G}')}\right) \begin{bmatrix} \hat{e}_2 \cdot \hat{e}'_2 & -\hat{e}_2 \cdot \hat{e}'_1 \\ -\hat{e}_1 \cdot \hat{e}'_2 & \hat{e}_1 \cdot \hat{e}'_1 \end{bmatrix} \quad (1.18)$$

and  $F\left(\frac{1}{\epsilon(\vec{G})}\right)$  is the Fourier transform of the inverse of  $\epsilon(\vec{G})$ .

The algebraic eigenvalue Equation 1.17 is solved for the eigenvalues to obtain the dispersion diagram.

### 1.3.3 Order-N method

The order-N method [1, 43, 44], essentially a finite element method, is based on the on-shell scattering method used in electron backscattering experiments [45]. It is a computationally efficient and stable method for calculating the dispersion of photonic crystal structures. In this method the space representing the dielectric distribution is discretized on a simple cubic mesh. The points on this mesh are defined using the lattice vectors  $\vec{a}$ ,  $\vec{b}$  and  $\vec{c}$ . The mesh of the  $\vec{E}$  and  $\vec{H}$  fields are displaced relative to each other as in

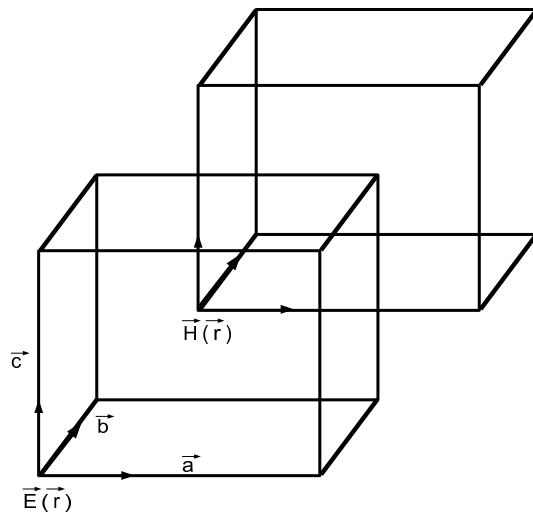


Figure 1.5: *Schematic of the electric and magnetic field meshes used in the order- $N$  method [1].*

Figure 1.5. In this method the integral form of the curl equations of Maxwell are used:

$$\oint \vec{E} \cdot d\vec{l} = -\frac{\partial}{\partial t} \int \vec{B} \cdot d\vec{S} \quad (1.19)$$

$$\oint \vec{H} \cdot d\vec{l} = \frac{\partial}{\partial t} \int \vec{D} \cdot d\vec{S} \quad (1.20)$$

The line integral of  $\vec{E}$  taken around the penetrating component of  $\vec{B}$  (as in Figure 1.6). gives

$$\vec{E}_1(\vec{r}) + \vec{E}_2(\vec{r} + \vec{a}) - \vec{E}_1(\vec{r} + \vec{b}) - \vec{E}_2(\vec{r}) = -\frac{\partial}{\partial t} \mu_0 \mu(\vec{r}) \vec{H}_3(\vec{r}) \quad (1.21)$$

Similar equations are obtained from the remaining components of Equations 1.19 and 1.20. These equations relate the field components on one side of the structure to that on the other side and is therefore the transfer matrix

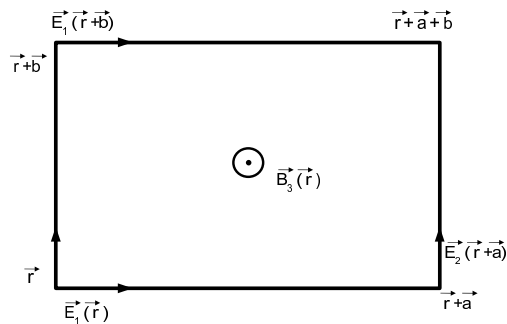


Figure 1.6: *Line integral of the electric field taken around the magnetic field (penetrating out of the plane of paper) .*

of the system. Computation of the fields at the points on one plane of the grid requires the field values on the previous plane. This method apart from being stable requires  $O(n)$  number of computations compared to  $O(n^3)$  computational steps in the plane wave expansion method. Moreover it can handle metals in the dielectric distribution. This method was later modified to use a generalized coordinate system and can be used to handle complex geometries.

### 1.3.4 Characteristic matrix approach

This method essentially applied to treat stratified media relates the fields on one side of the structured stratified media to that on the other side [46, 47]. It is used to determine propagation of a monochromatic plane wave across a layered structure. As shown in Figure 1.7 the field components on the left side ( $Q_0$ ) of the figure are expressed in terms of those on the right ( $Q_N$ ).  $M$  is called the characteristic matrix of the medium. The characteristic matrix of a homogeneous dielectric film stratified along the  $z$ -axis and using TE

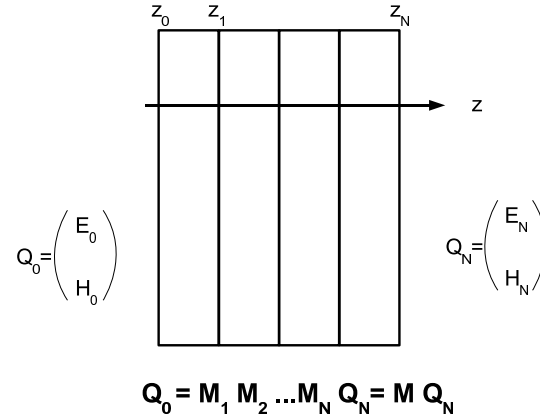


Figure 1.7: *The schematic of the characteristic matrix method.*

polarized light is given by [47]

$$M(z) = \begin{bmatrix} \cos(k_0 n z \cos \theta) & -\frac{i}{p} \sin(k_0 n z \cos \theta) \\ -ip \sin(k_0 n z \cos \theta) & \cos(k_0 n z \cos \theta) \end{bmatrix} \quad (1.22)$$

where

$$p = \sqrt{\frac{\epsilon}{\mu}} \cos \theta \quad (1.23)$$

$\epsilon$  is the dielectric constant of the film,  $\mu$  is the permeability,  $n = \sqrt{\epsilon\mu}$  is the refractive index,  $\theta$  is the angle of incidence and  $k_0$  is the wave number in free space. For the case of TM polarized light, the above equations hold on substituting  $p$  by

$$q = \sqrt{\frac{\mu}{\epsilon}} \cos \theta \quad (1.24)$$

For a structure of  $N$  stacked layers(as in Figure 1.7) located at  $z_0 \leq z \leq z_1$ ,  $z_1 \leq z \leq z_2$ , ...,  $z_{(N-1)} \leq z \leq z_N$ , the total characteristic matrix is given

as

$$M(z_N) = M(z_1)M(z_2 - z_1)\dots M(z_N - z_{N-1}) \quad (1.25)$$

A similar approach is the scattering matrix method where the coefficients of the field components approaching the stack are related to the coefficients of the field components propagating away from it [48]. The matrix elements of the scattering matrix and the characteristic matrix are therefore related.

For a characteristic matrix

$$M = \begin{bmatrix} m_{11} & m_{12} \\ m_{21} & m_{22} \end{bmatrix} \quad (1.26)$$

probability conservation and time reversal invariance give the following conditions

$$m_{11} = m_{22}^* \quad (1.27)$$

$$m_{21} = m_{12}^* \quad (1.28)$$

$$\det(M) = 1 \quad (1.29)$$

The reflection and transmission coefficients of the stack for the case of transverse electric polarization are

$$r = \frac{(m_{11} + m_{12}p_l)p_1 - (m_{21} + m_{22}p_l)}{(m_{11} + m_{12}p_l)p_1 + (m_{21} + m_{22}p_l)} \quad (1.30)$$

$$t = \frac{2p_1}{(m_{11} + m_{12}p_l)p_1 + (m_{21} + m_{22}p_l)} \quad (1.31)$$

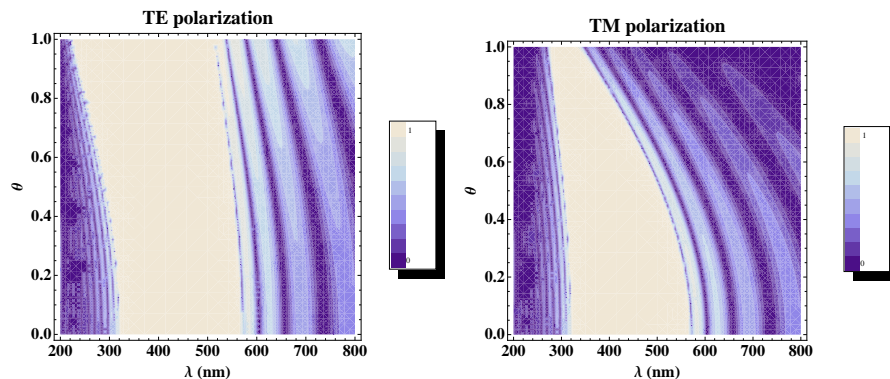


Figure 1.8: *The contour plot of reflectivity of 10 pairs of slabs with refractive indices 2.39 and 1.0 bounded on either side by air. The thickness of the individual slabs correspond to  $\lambda/4$  plates for normal incidence with  $\lambda=410\text{nm}$ . The angle of incidence is in radians.*

where  $p_1$  and  $p_l$  correspond to the values of Equation 1.23 in the first and the last media. The reflectivity is computed from Equation 1.30. As earlier,  $p_1$  and  $p_l$  substituted by  $q_1$  and  $q_l$  give the corresponding expressions for transverse magnetic polarization. It has been shown earlier (for example [48]) that only a finite number of slabs in the stack are sufficient for obtaining a saturated reflectivity profile. The Bragg frequency varies inversely as the square root of the average dielectric constant and the width of the reflectivity window is proportional to the refractive index contrast[49].

In Figure 1.8 the contour plot of the reflectivity of 10 pairs of slabs with refractive indices 2.39 and 1.0 placed alternately bounded on either side by air is shown. The thickness of the individual slabs correspond to  $\lambda/4$  plates for normal incidence with  $\lambda=410\text{nm}$ . The overlap of region of complete reflectivity of the TE and the TM polarizations corresponds to the photonic band gap of the photonic crystal stack. The calculation has

been done using Equation 1.30. It clearly shows the differing dispersion of the two polarizations. Such stacks can be used to design waveguides with lossless walls and owing to scalability of a photonic crystal structure, the scaled results hold as long as the dielectric constant of the material does not change with the frequency of incident radiation.

## 1.4 Conclusion

Conventional MMI devices and photonic band gap structures are actively being studied for device fabrication. Self-imaging though studied for conventional devices, still remains to be studied well for photonic band gap devices. With this background a study of a conventional MMI waveguide resonator, a critical coupling resonator and a MMI waveguide interferometer is presented subsequently in chapters 2, 3 and 4.

---

## A Dual Case I waveguide resonator with variable reflectivity mirrors

---

### 2.1 Introduction

There are three recognized low loss mirror configurations for waveguide laser resonators [12]. Consider a mirror of curvature  $R$  placed at a distance  $Z$  from the guide exit. In the Case I configuration, the mirror is either plane or of large radius of curvature and is placed close to the guide exit so that  $R^{-1} \approx 0$  and  $Z \approx 0$ . A dual case I design corresponds to having a Case I mirror at both ends of the waveguide. A Case II mirror will have its centre of curvature at the guide exit so that  $R = Z$ . Finally, for a Case III mirror,  $R = 2Z$  and  $Z$  equals the Rayleigh range  $\pi w^2/\lambda$  of a Gaussian beam (of waist  $w$ ) that has maximum overlap with the fundamental mode of the waveguide at the guide entrance. This occurs for a circular waveguide of radius  $a$ , when  $w/a = 0.64$ . The corresponding value for a waveguide of square cross section  $2a \times 2a$  is given by  $w/a = 0.7032$ . In each case, the power overlap is close to 98%.

Sometime ago, a new class of waveguide resonator was proposed [2] by exploiting the self imaging [50, 11, 51] properties of planar and rectangu-

lar cross-section step-index multimode waveguides. This design has many desirable properties: TEM<sub>00</sub> output, good mode suppression qualities, low round trip loss and robustness against perturbations such as mirror tilt. Furthermore, the design is more compact than either the case II or the case III design. In its simplest form, a self-imaging resonator is created by combining a multimode waveguide of square cross section  $2a \times 2a$  and length  $2a^2/\lambda$  (which produces a symmetric self-image on a single round-trip) with a Case I mirror at one end and a concave mirror placed near the other end. The concave mirror is placed at a distance  $Z = a^2/(2\lambda)$  from the guide exit and is phase matched to an effective TEM<sub>00</sub> beam of waist  $w_0 = 0.6a$ . Thus,  $R = Z + Z_0^2/Z$ , with  $Z_0 = \pi w_0^2/\lambda$ . The higher order mode suppression properties of this form of waveguide resonator and their physical origin have been described in earlier work [2, 52].

Although self-imaging resonators of the form described above are of great value, for example, in designing portable and robust CO<sub>2</sub> waveguide lasers with excellent transverse mode control, their implementation in semiconductor integrated optics technology is prohibited because of the need to form a concave reflecting surface. In practice, only cleaved facets whose planes are orthogonal to the axis of the laser waveguide are feasible in low cost mass production situations. From this perspective we consider a different implementation of the self-imaging resonator. The concept is based on providing higher order mode suppression by matching the peaks and nulls that occur in the transverse field patterns on the planar end facets

of the resonator with suitably colocated areas of high and low reflectivity, respectively.

The previous design of a waveguide resonator based on self-imaging [2] had the guide length, guide to mirror distance and the radius of the curved mirror parametrized by the guide-width and the operational wavelength. This made the previous design scalable to all wavelengths giving a new class of waveguide resonators. Similarly, the specifications of the new design, namely, the guide length and the dimensions of the high and low reflectivity regions of the mirrors require the guide width and the operational wavelength for their parametrization. Thus, the new design too is a new class of waveguide resonator based on self-imaging.

In a dual Case I design, the beam does not travel in free space before being coupled back into the waveguide with the higher order modes suppressed. No free space between the guide exit and the mirror makes the new design compact and reduces misalignment errors during installation of the mirrors at the exits of the waveguide as opposed to the Case I, II, III and the previous self-imaging based design [2].

## 2.2 Theory

### 2.2.1 Waveguide Modes

The modes of a rectangular cross sectioned waveguide are co-sinusoidal and separable in transverse co-ordinates. Furthermore, the corresponding prop-

agation constants can, under certain simplifying assumptions, be written as a sum of two terms, one for each transverse direction. Thus, the two-dimensional solution for the resonator field in Cartesian coordinates can be constructed from the solutions of two separate one dimensional descriptions of the resonator. Physically, it amounts to decomposing a rectangular cross sectioned waveguide into two planar waveguides.

The modes of a planar waveguide of width  $2a$  are of the form:

$$E_m(x, a) = \frac{1}{\sqrt{a}} \begin{cases} \cos(\pi mx/2a) & , \text{ if } m \text{ is odd;} \\ \sin(\pi mx/2a) & , \text{ if } m \text{ is even.} \end{cases} \quad (2.1)$$

These modes satisfy the orthogonality relation:

$$\int_{-a}^a E_m(x, a) E_n(x, a) dx = \delta_{mn} \quad (2.2)$$

The corresponding propagation constant is given by

$$k_m = \frac{2\pi}{\lambda} \left( 1 - \frac{1}{2} \left( \frac{m\lambda}{4a} \right)^2 \right) \quad (2.3)$$

so that the  $m$ -th mode propagating inside the waveguide along the  $z$ -direction will acquire a  $z$ -dependent phase factor, given by  $\exp(ik_m z)$  where,  $k_m = k - \beta_m$ ,  $k = 2\pi/\lambda$ ,  $\beta_m = \pi m^2/4L$  and  $L = 4a^2/\lambda$ . In what follows, we will ignore the mode-independent overall phase factor of  $\exp(ikz)$  as it does not affect our resonator mode calculations. In what follows, we discuss field propagation in the  $x$ - $z$  plane only as a similar analysis is valid in the  $y$ - $z$

plane also.

## 2.2.2 Self- Imaging and beam splitting

An arbitrary input field entering the waveguide at the  $z = 0$  plane can be expanded as

$$F(x, 0) = \sum_m a_m E_m(x, a) \quad (2.4)$$

At an axial distance  $z$  inside the waveguide, the input field becomes

$$F(x, z) = \sum_m a_m E_m(x, a) \exp(-i\beta_m z) \quad (2.5)$$

If we denote  $F$  by  $F_s$  when it is symmetric in  $x$  ( $m$  odd), by  $F_a$  when it is anti-symmetric in  $x$  ( $m$  even), and by  $F_g$  when it has no definite parity with respect to  $x$  ( $m$  both odd and even), then it is clear that

$$F_s(x, L) = F_s(x, 0) \exp(-i\pi/4), F_a(x, 2L) = F_a(x, 0), F_g(x, 8L) = F_g(x, 0) \quad (2.6)$$

Thus, the input field is *self-imaged* at a certain distance (called revival length) inside the waveguide.

At fractions of the revival length, the input field is split up into a finite number of its replicas. For example, it is easy to show that

$$F_a(x, L) = \frac{1}{2}[F_a(x + a, 0) + F_a(x - a, 0)] \quad (2.7)$$

Additionally,

$$F_s(x, L/2) = F_s(x - a/2, 0) + F_s(x + a/2, 0) \quad (2.8)$$

Our objective is to obtain a quasi-Gaussian output for the lowest loss mode of the waveguide resonator and to ensure that the more lossy solutions are sufficiently discriminated with respect to the lowest loss solution. In order to appreciate how we achieve this objective in the present design, it is instructive to review how it was done in the previous design.

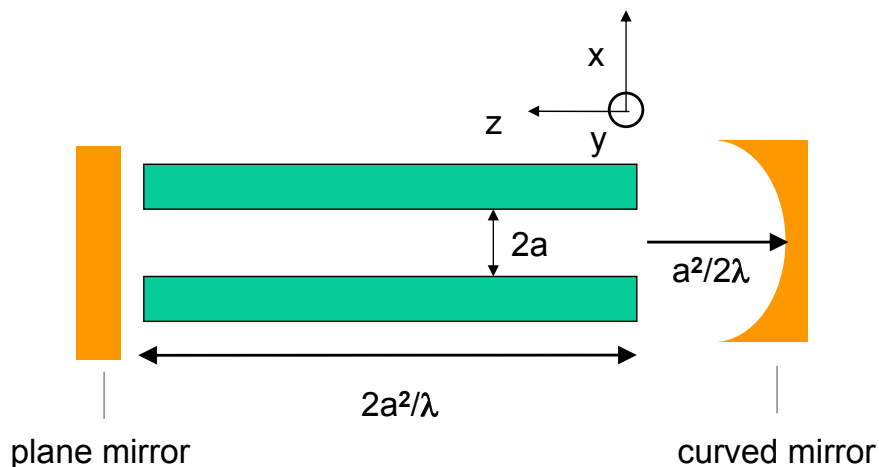


Figure 2.1: *Schematic of a self imaging waveguide resonator as reported in an earlier publication [2]. The resonator was formed of a waveguide of square cross section  $2a \times 2a$  and of length  $2a^2/\lambda = L/2$ , closed at one end ( $z = 0$ ) by a curved mirror at a distance  $a^2/2\lambda = L/8$  from the guide exit, and bounded at the other end ( $z = L/2$ ), by a plane mirror.*

## 2.3 Previous design and its working principle

The resonator was formed of a waveguide of square cross section  $2a \times 2a$  and of length  $2a^2/\lambda = L/2$ , closed at one end ( $z = 0$ ) by a curved mirror at a distance  $a^2/2\lambda = L/8$  from the guide exit, and bounded at the other end ( $z = L/2$ ), by a plane mirror as shown in Fig. 2.1.

Since the fundamental mode ( $m = 1$ ) of the waveguide is symmetric and is well approximated by a lowest order Gaussian beam of waist  $w = 0.7032a$  [53], a quasi-Gaussian output of the waveguide resonator is obtained in this design by the removal of (a) all anti-symmetric modes and (b) most (if not all) of the higher order symmetric modes in the following way.

In each round-trip, an anti-symmetric field suffers a two-way split at the edges of the guide exit ( $z = L/2$ ) in accordance with Eq. (2.8). This ensures high aperture loss on re-entry. A symmetric field, on the other hand remains unaffected by guided propagation according to the first of Eq. (2.6). Furthermore, the symmetric field is efficiently coupled back to the guide by the curved mirror which is phase matched to an effective  $\text{TEM}_{00}$  beam of waist  $\omega = 0.6a$  at the guide exit. The choice of this fictitious beam waist is to make sure that mostly the fundamental and a small amount of next order symmetric mode are allowed back into the waveguide. Thus the resonator operates mainly on the lowest order symmetric mode and filters out the unwanted anti-symmetric modes. Consequently, the resonator has a very low round trip loss. Moreover it was predicted to produce a  $\text{TEM}_{00}$ -like output with excellent mode discrimination even though the curved mirror was placed

much nearer to the guide exit (making the resonator more compact) than was conventional for achieving those results. Finally, the design parameters – guide length, guide to curved mirror distance and the mirror curvature – are functions of  $a$  and  $\lambda$  only. Since  $a$  and  $\lambda$  are arbitrary, a whole class of waveguide laser resonators can be fabricated.

## 2.4 Present Design and its working principle

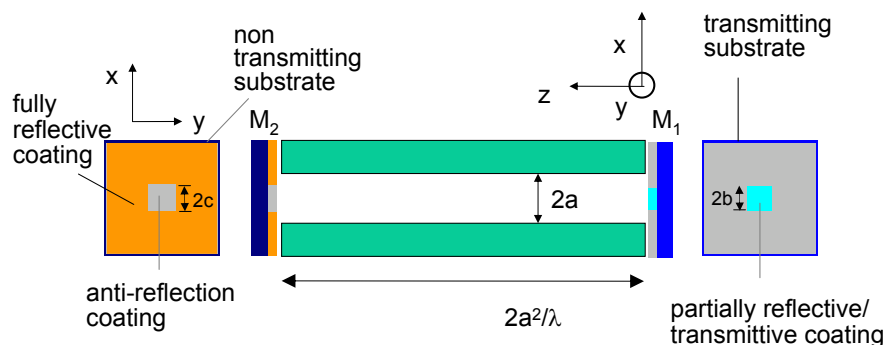


Figure 2.2: A new design for self-imaging waveguide resonators in which the end-mirrors are plane with step-reflectance profiles. We assume that the reflectivity of the mirror  $M_1$  at the ( $z = 0$ ) plane is  $r_1$  on a square block ( $2b \times 2b$ ) centered at the origin and  $r_2$  elsewhere with  $r_1 \approx 1$  and  $r_2 \approx 0$ . The reflectivity of the mirror  $M_2$  at the ( $z = L/2$ ) plane, on the other hand, is taken to be  $r_2$  on a square block ( $2c \times 2c$ ) centered at the origin and  $r_1$  elsewhere.

In the present design, both resonator mirrors are plane with suitably chosen variable reflectivity profiles as shown in Fig. 2.2. We assume that the

reflectivity of the mirror  $M_1$  at the ( $z = 0$ ) is  $r_1$  on a square block ( $2b \times 2b$ ) centered at the origin and  $r_2$  elsewhere with  $r_1 \approx 1$  and  $r_2 \approx 0$ . The reflectivity of the mirror  $M_2$  at the ( $z = L/2$ ) plane, on the other hand, is taken to be  $r_2$  on a square block ( $2c \times 2c$ ) centered at the origin and  $r_1$  elsewhere.

Before proceeding, it is important to note that in this design, there is no free space region and no focusing element such as a curved mirror. Thus the resonator solutions will be composed of many waveguide modes. In this design, the nature of the resonator mode is defined by the spatial reflectivity profiles of the plane mirrors and the self-imaging and splitting properties of the multimode waveguide.

We start by writing the resonator mode in the  $z = 0$  plane, propagating in the  $+z$  direction, in terms of waveguide modes as in (2.4):

$$F_0(x, 0) = \sum_m a_m E_m(x, a) \quad (2.9)$$

In one round trip, the field propagates to the  $Z = L/2$  plane, and reflects off mirror  $M_2$ . Then, it returns to the  $z = 0$  plane and reflects off mirror  $M_1$ . Thus, after one round trip, the initial field distribution  $F_0(x, a)$  will transform to the following distribution:

$$F_1(x, a) = \sum_{m,n,p} a_m \exp(-i\beta_m L/2) X_{mn}^{(2)} \exp(-i\beta_n L/2) X_{np}^{(1)} E_p(x, a) \quad (2.10)$$

where,  $X_{mn}^{(i)}$  is the coupling amplitude between the waveguide modes  $E_m$  and

$E_n$  due to reflection from the mirror  $M_i$ . Equating  $F_1(x, a)$  to  $F_0(x, a)$  within a multiplicative factor  $\sigma$  and using the orthogonality relation, we obtain the matrix equation

$$\sum_{m,n} X_{qn}^{(1)} \exp(-i\beta_n L/2) X_{nm}^{(2)} \exp(-i\beta_m L/2) a_m = \sigma a_q \quad (2.11)$$

The eigenvectors and the eigenvalues of Eq. 2.11 are used to obtain the resonator mode profiles and their round-trip loss factors.

For step-index reflectivity profiles, one can easily calculate the mirror coupling amplitudes. One gets

$$\begin{aligned} X_{mn}^{(1)} &= \left[ r_2 \left( \int_{-a}^{-b} dx + \int_b^a dx \right) + r_1 \int_{-b}^b dx \right] E_m(x, a) E_n(x, a) \\ &= r_2 \delta_{mn} + (r_1 - r_2) I_{mn}(c) \end{aligned} \quad (2.12)$$

where,

$$I_{mn}(b) = \int_{-b}^b E_m(x, a) E_n(x, a) dx \quad (2.13)$$

and,

$$\begin{aligned} X_{mn}^{(2)} &= \left[ r_1 \left( \int_{-a}^{-c} dx + \int_c^a dx \right) + r_2 \int_{-c}^c dx \right] E_m(x, a) E_n(x, a) \\ &= r_1 \delta_{mn} - (r_1 - r_2) I_{mn}(b) \end{aligned} \quad (2.14)$$

The expression for  $I_{mn}(b)$  can be evaluated easily. One gets

$$I_{mn}(b) = \begin{cases} \gamma_{m-n}(b/a) - \gamma_{m+n}(b/a) & , \text{ if } m \text{ and } n \text{ are both even} \\ \gamma_{m-n}(b/a) + \gamma_{m+n}(b/a) & , \text{ if } m \text{ and } n \text{ are both odd} \\ 0 & , \text{ otherwise} \end{cases} \quad (2.15)$$

where,

$$\gamma_j(x) = \begin{cases} \frac{\sin(\pi j x/2)}{\pi j/2} & , \text{ for } j \neq 0 \\ x & , \text{ otherwise} \end{cases} \quad (2.16)$$

## 2.5 Results and Discussion

For the sake of simplicity, we begin by assuming that a high reflectivity segment does not transmit and a low reflectivity segment does not reflect. That is, we set  $r_1 = 1$  and  $r_2 = 0$ . In reality, the mirror at the ( $z = 0$ ) plane acts as the output mirror and thus, is partially transmittive. We will later show that our arguments remain valid even for more realistic reflectivity profiles.

Let us start by assuming that the mirror at the  $z = L/2$  plane is fully reflective, i.e.  $c = 0$  whereas the mirror at the  $z = 0$  plane has a  $2b \times 2b$  segment of high reflectivity at the origin and low reflectivity elsewhere. The mirror segments of high reflectivity are needed to support the symmetric modes at each end with negligible loss and to reproduce them after each round-trip according to the first of Eq. (2.6). On the other hand, the mirror segments of low reflectivity at the  $z = 0$  plane would ensure, according to Eq.

(2.7), that the anti-symmetric modes suffer significant losses on reflection in each round trip. Thus, at steady state (in the sense of Fox and Li [54]), the resonator field would comprise only of symmetric modes. In other words, if the  $n$ -th resonator mode is written in terms of waveguide modes as  $R_n(x) = \sum_m c_m^{(n)} E_m(x, a)$ , then, only odd values of  $m$  would appear in the sum.

If the anti-symmetric modes are filtered out at the  $z = 0$  plane by the mirror segments of low reflectivity, then the resonator modes will comprise of symmetric waveguide modes and will, therefore have a symmetric nature themselves. Since any symmetric field is reproduced after propagating a round-trip distance  $L$ , all these symmetric solutions will have zero loss. In order to lift this degeneracy, some further transverse field filtering is

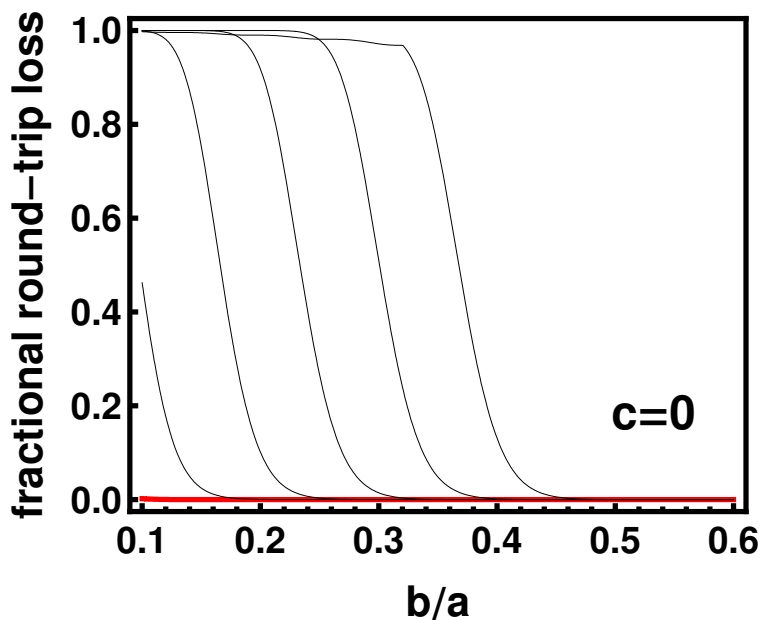


Figure 2.3: Round-trip fractional loss of the first six resonator modes (all of which are symmetric solutions) in the  $x$ - $z$  plane as a function of  $b/a$  when  $c = 0$ . The thick red line corresponds to the lowest-loss mode. All the calculations have been carried out in Mathematica 6.0.

necessary. This is where the width of the mirror segments come into play. In Fig. 2.3, we plot the round trip fractional loss of the first six resonator modes (all of which are symmetric solutions) as a function of  $b/a$  when  $c = 0$ .

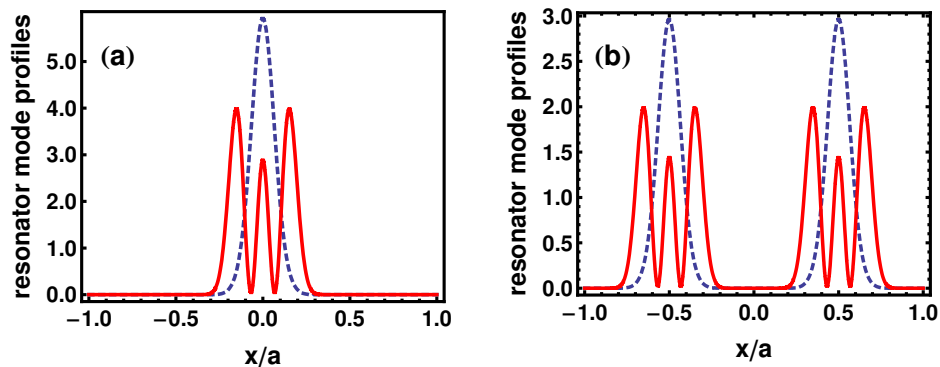


Figure 2.4: Profiles for the two lowest loss resonator modes in the  $x$ - $z$  plane at (a)  $z = 0$  and at (b)  $z = L/2$  when  $b/a = 0.44$  and  $c = 0$ . The dotted line corresponds to the lowest loss mode whereas the solid line corresponds to the other mode.

Clearly, if the mirror width is reduced sufficiently, even the symmetric solutions become lossy. This process starts at about  $b/a \approx 0.45$  when a quasi-Gaussian solution emerges and continues as  $b/a$  is reduced further. The loss arises due to aperturing at the mirror edges as the non-Gaussian symmetric modes of the resonator tend to spread out near the wings. In Fig. 2.4, we show the resonator mode profiles at each mirror for  $b/a = 0.44$  and  $c = 0$ .

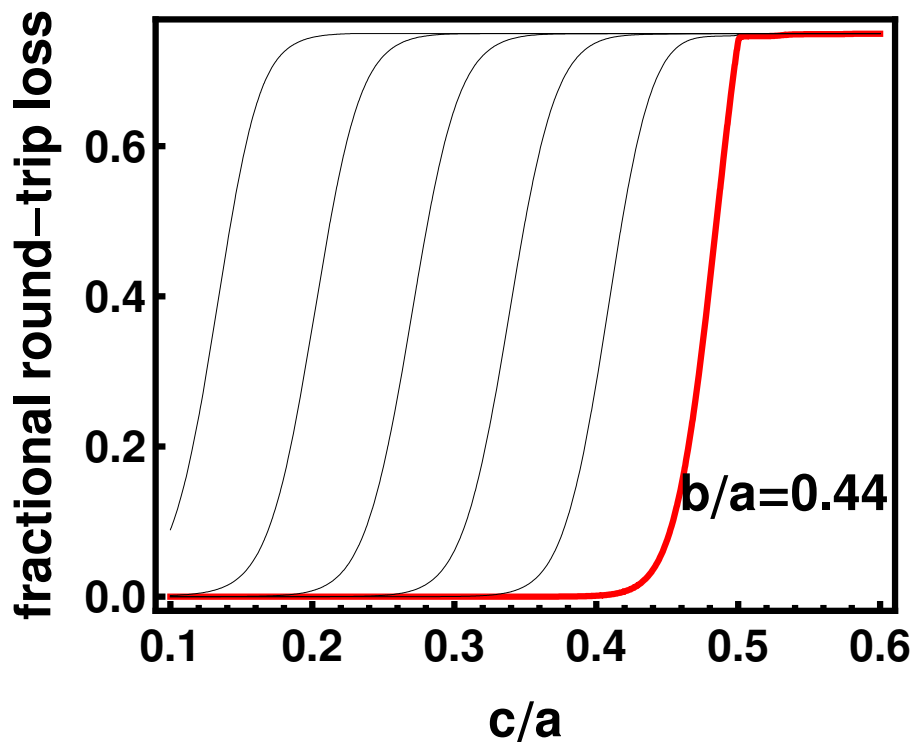


Figure 2.5: *Round-trip fractional loss for the first six resonator modes (in ascending order of fractional loss) in the  $x$ - $z$  plane, as a function of  $c/a$  when  $b/a = 0.44$ . The thick red line corresponds to the lowest-loss mode.*

An ideal resonator mode should have a quasi-Gaussian nature and provide a good overlap with the gain medium. From this perspective we fix the value of  $b/a$  at 0.44. Additional loss can be induced for the non-Gaussian modes by aperturing them at the  $z = L/2$  plane without disturbing the two-way split of the quasi-Gaussian solution. This would mean increasing the value of  $c$  from zero to some finite value such that sufficient mode discrimination arises between the lowest-loss quasi-Gaussian solution and the lossier Gaussian solutions.

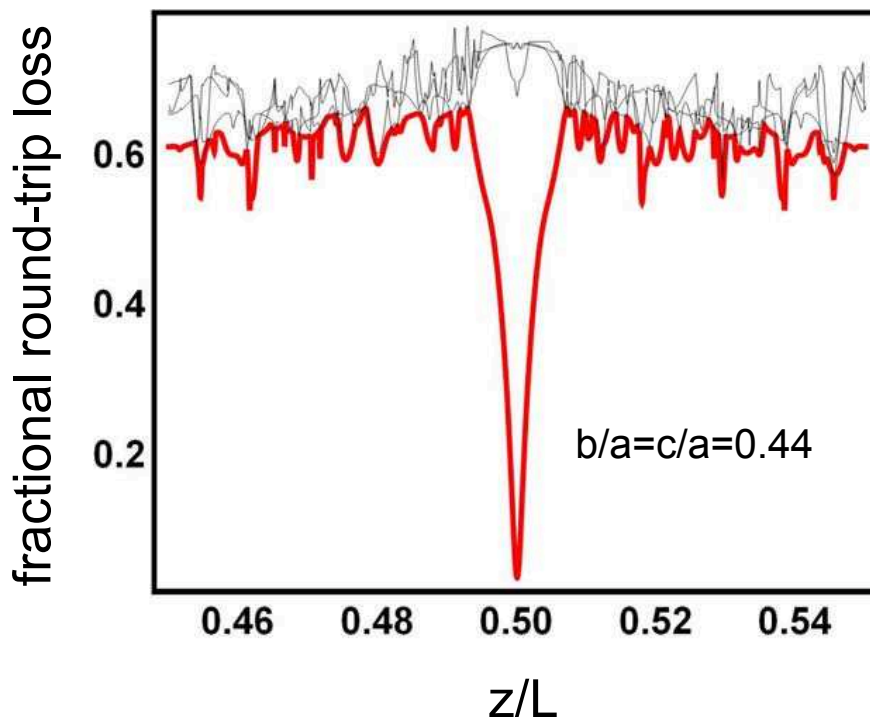


Figure 2.6: *Round-trip fractional loss for the first six resonator modes in the  $x$ - $z$  plane as a function of the resonator length when  $b/a = c/a = 0.44$ . The thick red line corresponds to the lowest-loss mode.*

In Fig. 2.5, we plot round-trip fractional loss for the first six resonator solutions as a function of  $c/a$  when  $b/a = 0.44$ . It is clearly seen that there is a small window around  $c/a \approx 0.45$  where all but the lowest-loss mode suffer substantial losses. Further calculations indicate that there is a sizable window in the range  $0.4 \leq b/a = c/a \leq 0.45$ , where the fundamental resonator mode has substantially lower loss than other solutions. In Fig. 2.6, we show the sensitivity of the solution for  $b/a = c/a = 0.44$  against variations in the resonator length.

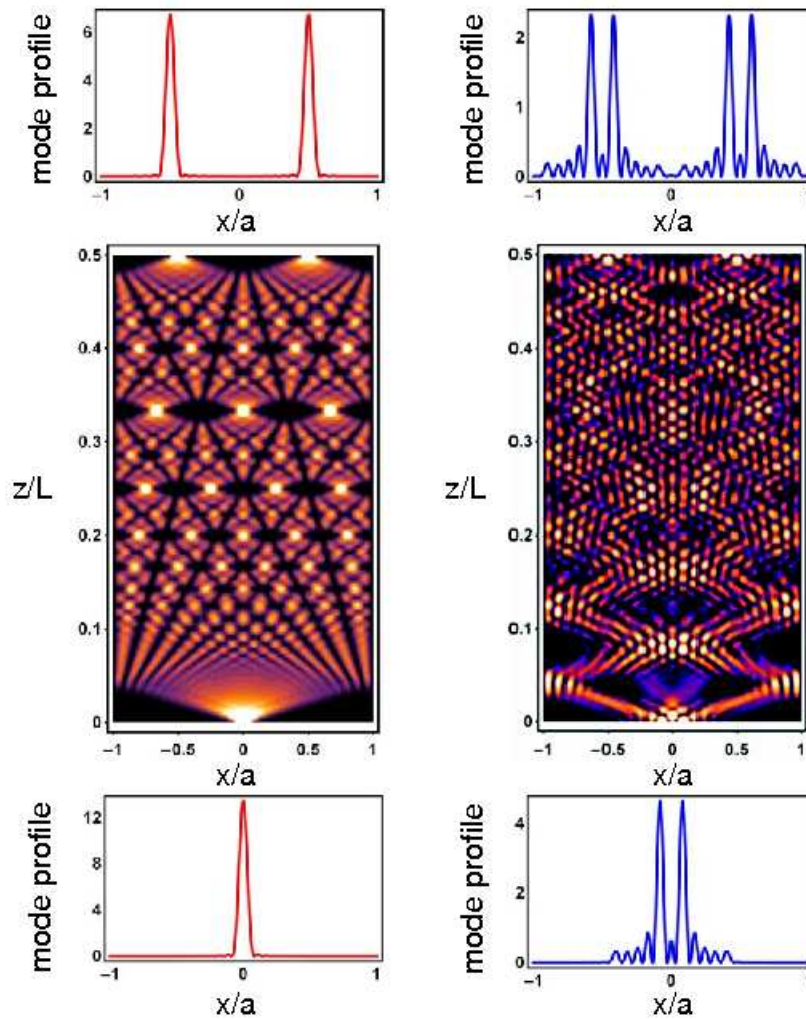


Figure 2.7: *The transverse intensity profiles in the  $x$ - $z$  plane, at each end of the resonator and inside the waveguide for the two lowest loss resonator modes when  $b/a = c/a = 0.44$  and the resonator length is set at  $L/2 = 2a^2/\lambda$ . The left column represents the profiles for the lowest-loss mode in the  $+z$  direction, and the right column represents the profiles for the next mode (in ascending order of fractional loss). In each column, the bottom figure displays the intensity profile at  $z = 0$ , the middle figure is the contour plot of the intensity profile inside the waveguide, and the top figure is the intensity profile at  $z = L/2$ .*

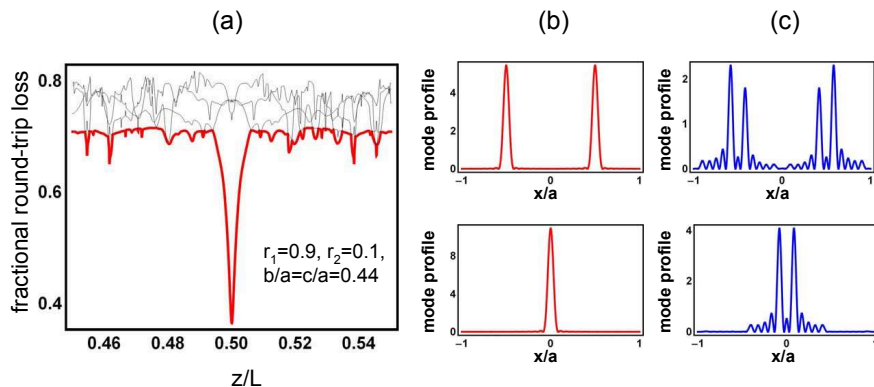


Figure 2.8: The mirror reflectivity is set at 0.9 for the high-reflectivity segments and at 0.1 for the low reflectivity segments. (a) Round-trip fractional loss for the first six resonator modes in the  $x$ - $z$  plane as a function of the resonator length. All other details are as in Fig. 2.6. (b) Intensity profiles for the lowest-loss mode at  $z = 0$  (bottom figure) and  $z = L/2$  (top figure). (c) The same as in (b) for the next mode (in ascending order of fractional loss).

In Fig. 2.7, we show the transverse intensity profiles in the  $x$ - $z$  plane at each end of the resonator and inside the waveguide for the two lowest loss resonator modes when  $b/a = c/a = 0.44$  and the resonator length is set at  $L/2 = 2a^2/\lambda$ . Before ending we note that for realistic mirrors, the reflectivity is neither 100%, nor 0%. In Fig. 2.8, we show that our main findings remain valid even for realistic mirror reflectivities.

## 2.6 Conclusion

In summary, we have described the design and working principle of a multi-mode waveguide resonator that is predicted to yield quasi-Gaussian output with low round-trip loss and excellent mode discrimination as obtained in

our earlier design of a self-imaging waveguide resonator[2].

The novelty in the present design is that the above desirable properties are secured by the use of end mirrors with suitable step-index reflectivity profiles in a *dual Case I configuration*, that is, with plane mirrors and without any free space region between the waveguide and the mirrors. Thus, the resonator will have the advantages of being compact and portable. It should also be easy to fabricate even in semiconductor integrated optics technology where curved reflecting mirrors are prohibitively difficult to implement whereas plane mirrors can be mimicked by cleaved facets.

---

## 3 Critical coupling at oblique incidence

---

### 3.1 Introduction

The analysis of a system called the critical coupling resonator is presented in this chapter. A critically coupled resonator (CCR) consists of a thin absorbing film capable of absorbing nearly all of the incident radiation on it. The arrangement is sketched in Fig. 3.1. The absorbing film is only about a nanometers thick and can consist of any material with a high absorption coefficient. The absorbing film is separated from a reflecting structure by a dielectric layer called the spacer layer.

Composite media have attracted the attention of researchers for the past few decades for their exotic properties [55, 56, 57, 58, 59, 60, 61], quite distinct from those of the bulk constituents. For example, metal nano particles in a dielectric host can support the so-called particle plasmons or the Mie plasmons [55, 56, 57, 62]. These resonances are absent in the bulk metal or in the dielectric constituent. Excitation of the Mie plasmons is associated with large local field enhancement, which is quite promising for various different areas ranging from nonlinear optics, surface enhanced spectroscopy to bio

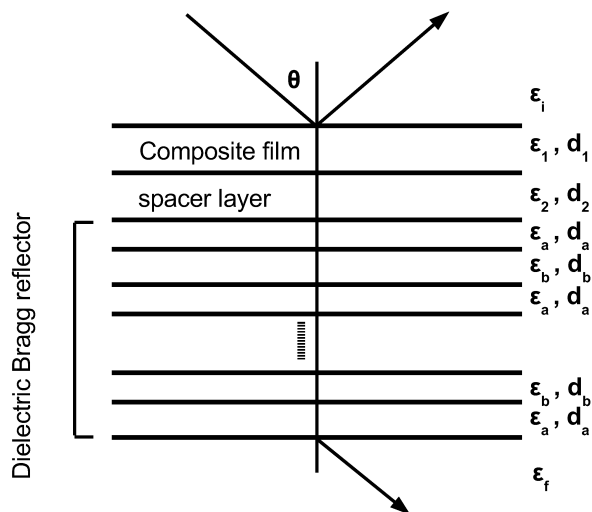


Figure 3.1: *Schematic diagram of the layered medium.*

imaging and drug delivery [60, 63, 64, 65, 66]. In the context of a composite medium, the important parameter that controls its properties is the volume fraction of the metal inclusions. In fact, a change in the volume fraction can tune the location of the Mie plasmons as well as control its oscillator strength (peak absorption). Such flexibilities of a composite medium have been exploited in optical limiting, pulse velocity control and many other applications [60, 63, 64]. Recently it was shown that a thin nano layer of a metal-dielectric composite separated from a distributed Bragg reflector (DBR) by a dielectric spacer layer can exhibit critical coupling [67]. In fact, critical coupling leading to almost complete absorption in a 5 nm thick lossy J-aggregated film (with large oscillator strength) in a similar geometry was first demonstrated by Tischler et al [68, 69]. It is clear that almost perfect absorption of the incident light energy by the nano film leads to virtually null transmission and reflection at a given frequency. The simultaneous

cancellation of both reflection and transmission results as a consequence of a very delicate interplay of the counter propagating waves in the layers. The use of the composite layer had the added advantage that one could control the critical coupling frequency. Moreover, it was shown that it is possible to achieve critical coupling at two distinct frequencies for large oscillator strengths of the Mie plasmons (for large volume fraction) [67]. Note that critical coupling is not the only means of achieving perfect absorption. Other mechanisms (Brewster effect and excitation of surface plasmons) involving shallow and deep metallic gratings have been exploited in the past for almost total absorption of incident light [70, 71].

All the previous studies on critical coupling involving absorbing nano layers were restricted to normal incidence of plane polarized light [68, 69, 67]. It is of interest to investigate whether such effects persist in the case of oblique incidence. Besides, for oblique incidence one needs to distinguish between the TE or TM polarizations, whereas, for normal incidence both are the same. In this paper, we study critical coupling in a multilayered system (see Figure 3.1) comprising of a composite nano film, a spacer layer and a DBR under oblique incidence of TE or TM polarized plane wave. We show that it is possible to minimize simultaneously both reflection and transmission from the structure for both the polarizations. Thus even at oblique incidence critical coupling can be achieved leading to almost total absorption of the incident energy in the composite film. Large oscillator strengths (large  $f$ ) are again shown to lead to critical coupling at two distinct frequencies for each

polarization. We further demonstrate that the reflection and transmission profiles for the TM polarization have distinctive features that are absent in the TE case. In fact, they exhibit additional resonances which can be traced to the excitation of the longitudinal bulk plasmons in the composite film.

The structure of the chapter is as follows. In Section 3.2, we recall some basic properties of the composite media, describe our system and formulate the problem. In the next Section (Section 3.3), we present the numerical results. Finally, in Section 3.4 we summarize the important results.

## 3.2 Mathematical Formulation

Consider the system shown in Figure 3.1, where a thin metal-dielectric composite film is deposited on a spacer layer which resides on top of a DBR. The whole structure is grown on a silica substrate and illuminated from the top by TE or TM polarized plane wave at an angle  $\theta$ . The DBR consists of  $2N+1$  layers with alternating dielectric constants  $\epsilon_a$ ,  $\epsilon_b$  and widths  $d_a$ ,  $d_b$ , respectively. It is quite clear from the previous studies [68, 69, 67] that critical coupling can be realized when the composite absorption frequency lies inside the band-gap of the DBR. For a structure with fixed parameters of the DBR (i.e., widths and dielectric functions), an increase in the angle of incidence will lead to a shift of the band-gap to lower wavelengths, while the absorption dip of the composite will remain unaffected. Eventually the absorption frequency may be outside the band-gap leading to the loss of critical coupling. Keeping this in view, we use different sets of values of  $d_a$

and  $d_b$  such that each sublayer of the DBR correspond to a  $\lambda/4$  plate at each specified angle of incidence  $\theta$  resulting in a central Bragg frequency at  $\lambda_c = 410nm$ . We thus choose  $d_a, d_b$  as follows

$$d_{a,b} = \frac{\lambda_c}{4n_{a,b} \cos \theta_{a,b}}, \theta_{a,b} = \sin^{-1} \left[ \frac{n_i}{n_{a,b}} \sin \theta \right] \quad (3.1)$$

where  $n_i = \sqrt{\epsilon_i}$  and  $n_{a,b} = \sqrt{\epsilon_{a,b}}$ .

In what follows, we briefly discuss the composition of the composite medium and recall some of its important properties. Let the composite medium consist of silver (with dielectric function  $\epsilon_m$ ) nano-particles in a silica host (with dielectric function  $\epsilon_h$ ). The properties of such metal nano-particle composites have been discussed in detail by many [56, 57]. It was shown by Niklasson [61] that effective medium theories, in particular, Maxwell-Garnett(MG) [56] theory can be applied effectively for particle sizes upto 9-10 nm in the visible range. One needs to exercise caution for dealing with metal composites in the presence of excitation of Mie plasmons. MG theory works well in the absence of large variation of the field for quasistatics to hold. This is usually not the case when Mie plasmons (with local field enhancement near the nano-particles) are excited. In situations where the field enhancement is not too large, we assume that MG theory can be applied and one can write down the effective dielectric function of the composite as follows

$$\epsilon_1(\omega) = \epsilon_h + \frac{fx(\epsilon_m - \epsilon_h)}{1 + f(x - 1)}, x = \frac{3\epsilon_h}{\epsilon_m + 2\epsilon_h} \quad (3.2)$$

where  $f$  is the volume fraction. In order to highlight the qualitative differences of the composite material from the bulk metal we have plotted the real and imaginary parts of the dielectric function in Figure 3.2. We have used

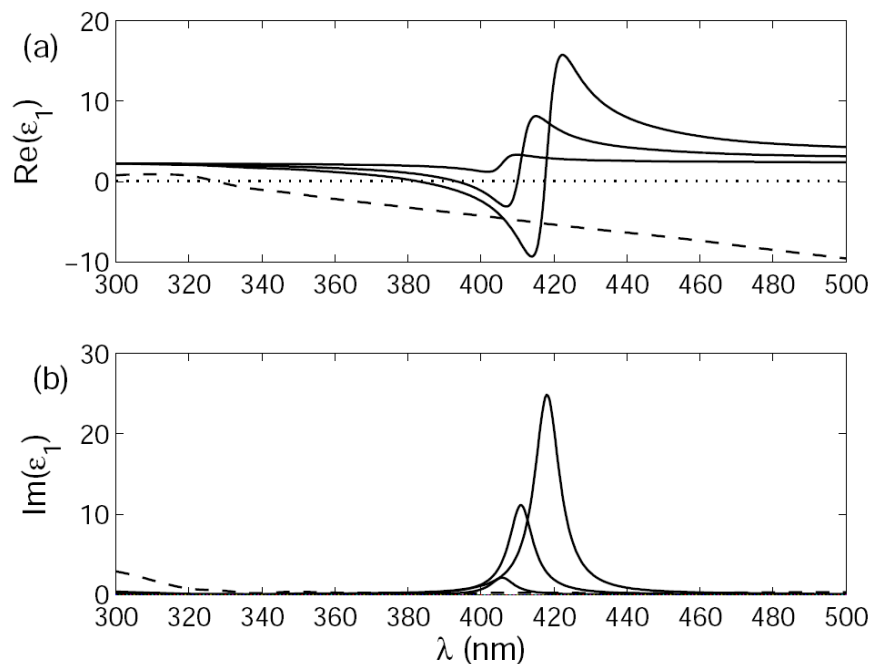


Figure 3.2: *Real and Imaginary parts of the complex dielectric function for the composite material. Curves from top to bottom are for  $f = 0.1$ ,  $0.05$  and  $0.01$  respectively. The dashed curve corresponds to bulk metal ( $f = 1.0$ ).*

the interpolated Johnson and Christy [72] data for  $\epsilon_m$  for all calculations. The same are reproduced in Figures 3.2(a) and 3.2(b) by dashed lines for comparison. Note that the bulk data for silver can be used for nano-particles of sizes down to 4 nm [73]. It is clear from Figure 3.2 that bulk silver does not exhibit any resonance features at around 400 nm, while the composite shows prominent Mie plasmon resonances. The other important feature that needs to be noted from Figure 3.2 is the crucial dependence of these resonances

on the volume fraction  $f$ . Indeed the resonance frequency shifts to the right along with an increase in the oscillator strength (peak absorption) with an increase in  $f$ . One should also note the metal like behavior ( $Re(\epsilon) < 0$ ) of the composite around  $\lambda = 405nm$ , which is responsible for critical coupling at one or more frequencies.

It is pertinent to make a few comments on the applicability of Equation 3.2 for the composite nanofilm in presence of Mie resonances. It is clear that the applicability of a formula (Equation 3.2), derived in quasi-static approximation, is questionable in presence of strong Mie resonances. In this paper we use Equation 3.2 as an approximation. We tested the applicability of Equation 3.2 for the samples of Shatabdi et al [64]. The location of the resonance predicted by Equation 3.2 (see the curve for  $f = 1.0$  in Figure 3.2(b)) matches well with the experimental results on the nanofilms [64]. Thus MG theory seems to work even in presence of Mie resonances, provided that the field enhancement associated with these resonances are not very significant. A similar model used in a different context yielded nice matching with the experimental findings [74]. The second comment relates to the applicability of Equation 3.2, which was derived for bulk samples, to a quasi two-dimensional nano film. Of course the quasi two-dimensional nature of the composite film will lead to deviations of the effective index from Equation 3.2. In fact, the thin film can behave like a uniaxial anisotropic medium with the uniaxis perpendicular to the layers [74, 75]. However, we neglect all these effects since they do not affect the underlying physics and the main effects,

which are presented in the next section. In other words, even in presence of deviation of the true response from this model, the basic results of this paper still will hold, albeit with a readaptation of the optogeometrical parameters.

### 3.3 Numerical Results and Discussions

In this section we present numerical results pertaining to the reflection and transmission coefficients for oblique incidence of TE or TM polarized light. The same can be calculated using the characteristic matrix or the transfer matrix technique [57, 46]. For numerical calculations, the following parameters were chosen:  $N = 10$ ,  $\epsilon_i = 1.0$ ,  $\epsilon_h = 2.25$ ,  $\epsilon_f = 2.25$ ,  $\epsilon_2 = 2.6244$ ,  $\epsilon_a = 5.7121$  and  $\epsilon_b = 2.6244$ . We first pick a structure which exhibits critical coupling for normal incidence [67] with  $d_1 = 10nm$ ,  $d_2 = 75nm$  and  $f = 0.05$ . We show that at oblique incidence the critical coupling is lost even though the scaled (as per Equation 3.1)  $d_a$ ,  $d_b$  values are used so as to have the central Bragg frequency at 410 nm. These are shown in Figures 3.3(a) and 3.3(b) for TE and TM polarization. We have plotted total scattering  $R + T$  as functions of wavelength for three different angles of incidence, namely,  $\theta = 0^\circ, 45^\circ$  and  $60^\circ$ , respectively. A comparison of the two panels in Figure 3.3 reveals that for larger angles it is easier to maintain critical coupling for TM polarized light.

We next show that critical coupling at a given angle of incidence can be recovered by adjusting the parameters of the layered medium. Like in the case of normal incidence, the critical coupling can also be optimized by

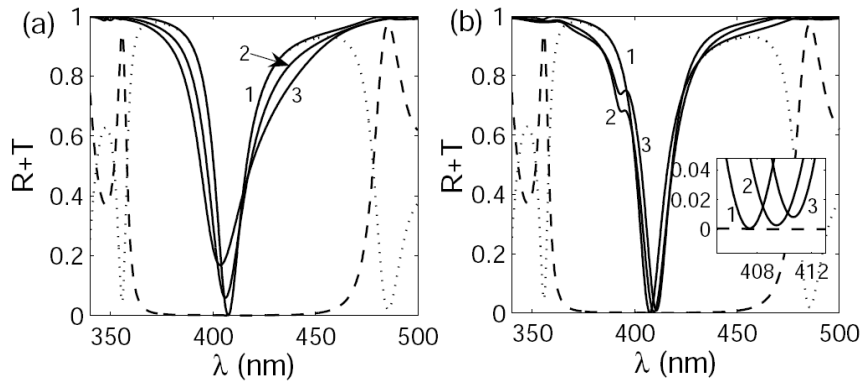


Figure 3.3: Total scattering  $R + T$  (solid lines) as functions of wavelength  $\lambda$  for (a) TE and (b) TM polarization for  $d_1 = 10$  nm,  $d_2 = 75$  nm and  $f = 0.05$ . Curves marked by 1, 2 and 3 correspond to  $\theta = 0^\circ$ ,  $45^\circ$  and  $60^\circ$ , respectively. The inset shows a magnification near  $R + T = 0$ . Other parameters are  $N = 10$ ,  $\epsilon_i = 1.0$ ,  $\epsilon_h = 2.25$ ,  $\epsilon_f = 2.25$ ,  $\epsilon_a = 5.7121$ ,  $\epsilon_b = 2.6244$ . The normal incidence transmission and reflection for the total structure are also shown by dashed and dotted lines, respectively.

changing the spacer layer thickness. This is shown in Figures 3.4(c) (for TE) and 3.4(d) (for TM) for  $d_1 = 10$  nm,  $f = 0.05$  and for  $\theta = 45^\circ$ . Curves 1, 2 and 3 in (c) are for  $d_2 = 30, 45$  and  $65$  nm, respectively, while those in (d) correspond to  $d_2 = 30, 51$  and  $65$  nm. For reference we have also shown the reflection (solid line) and transmission (dashed line) coefficients of the bare composite film on the substrate for TE (Figure 3.4(a)) and TM (Figure 3.4(b)) incidence. It is clear from figures 3.4(c) and 3.4(d) that absorption in the composite film can be optimized for  $d_2 = 44$  nm (51 nm) for TE (TM) polarization. A very interesting feature characteristic of only the TM polarization emerges if one compares the left and right panels of Figure 3.4. Indeed the transmission through the composite film (Figure 3.4(b)) for the TM case has an additional resonance dip around  $\lambda = 393$  nm just on the

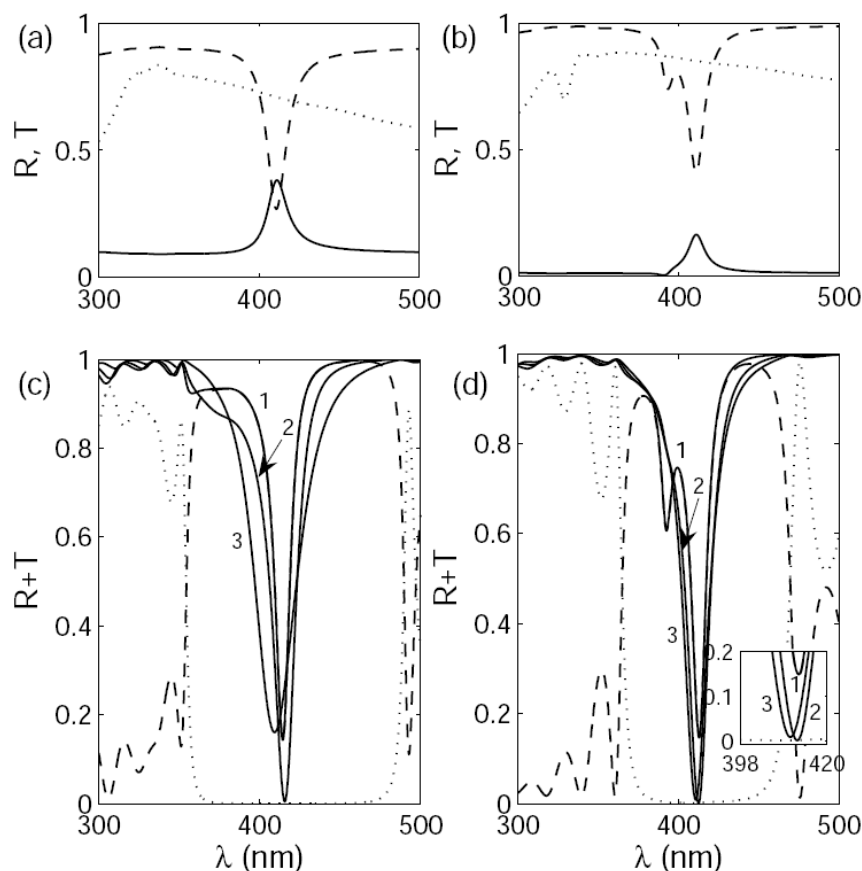


Figure 3.4: *Oblique incidence (at  $\theta = 45^\circ$ ) transmission (dashed line) and reflection (solid line) of the bare composite film with  $f=0.05$ ,  $d_1=10$  nm on the substrate for (a) TE and (b) TM polarizations. The transmission for  $f=1.0$  (dotted line) is shown for reference on both the panels. Oblique incidence (at  $\theta = 45^\circ$ ) total scattering  $R + T$  (solid lines) as functions of  $\lambda$  for  $d_1=10$  nm,  $f=0.05$ , for (c) TE polarization with  $d_2=30$ , 45 and 65 nm (curves 1, 2 and 3, respectively) and for (d) TM polarization with  $d_2=30$ , 51 and 65 nm (curves 1, 2 and 3, respectively). The inset in 4(d) shows a magnification near  $R + T = 0$ . Other parameters are as in Figure 3.3.*

left of the Mie plasmon resonance at  $\lambda = 412$  nm. Such features show up in the total scattering from the structure  $R+T$  in figure 3.4(d) (also in figure 3.3(b), albeit at a slightly different frequency). In fact the location of this resonance

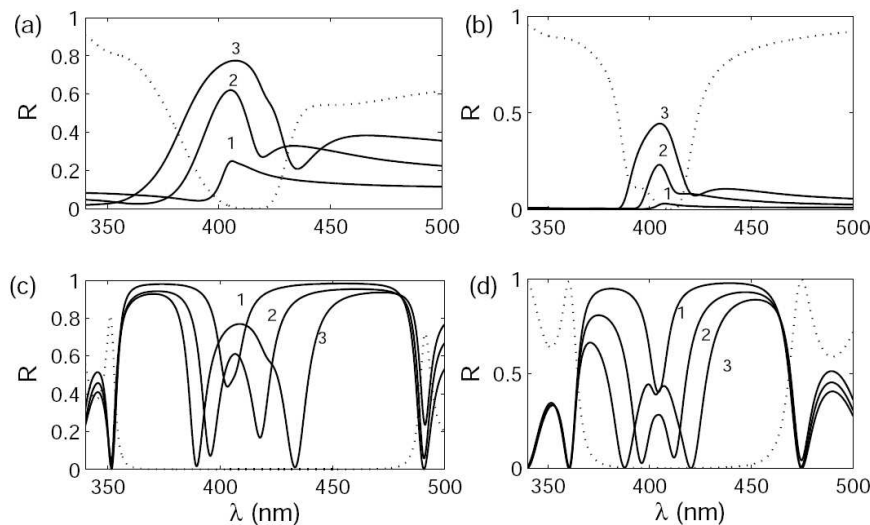


Figure 3.5: *Oblique incidence (at  $\theta = 45^\circ$ ) intensity reflection as a function of  $\lambda$  for a 70 nm thick composite film on a substrate ((a) and (b)) and for the total structure ((c) with  $d_2=85$  nm and (d) with  $d_2=98$  nm). The left panels ((a) and (c)) are for TE incidence, while the right ones ((b) and (d)) are for TM. Curves 1, 2 and 3 in the left panels correspond to  $f=0.01$ ,  $0.05$  and  $0.1$ , respectively, while those on the right correspond to  $f=0.01$ ,  $0.03$  and  $0.06$ , respectively. The transmission (dotted line) is shown for reference with  $f=0.1$  for TE and with  $f=0.06$  for TM polarization. Other parameters are as in Figure 3.3*

is insensitive to the angle of incidence or even the widths of the composite or the spacer layers. The only parameter that governs its location is the volume fraction of the inclusions in the composite material. One can explain the origin of this resonance if one recalls the work in the sixties on longitudinal bulk plasmons in thin metal films for oblique incidence [76]. Excitation of bulk plasmons requires essentially a non-vanishing electric field component normal to the interface. It is thus clear that normally incident light or TE polarized light at oblique incidence cannot excite such longitudinal plasmons. It is also evident that such excitations can be supported by the composite film

only when it exhibits metal like behavior (for large  $f$ ). In order to verify that the resonance feature is indeed due to the longitudinal plasmons, we looked at the limiting case when  $f = 1.0$ . This limit corresponds to the situation when the top layer represents a homogeneous silver film. With an increase in  $f$  the left dip at 393 nm (see dashed line in Figure 3.4(b)) moves towards lower wavelengths (not shown) finally merging with the usual plasmon dip at around  $\lambda = 328$  nm for a homogeneous silver film (see dotted line in Figure 3.4(b)). Note that such a dip is absent in the transmission profile of the film for TE polarized light (dotted line in Figure 3.4(a)).

It was pointed out earlier that for large volume fraction leading to large oscillator strength of the Mie plasmons, the composite film can exhibit metal like behavior in a narrow frequency window (see the region below the dotted line in Figure 3.2(a)). On the two edges of this window, the refractive index has very low or high values leading to a large difference of round trip phase in the composite film [67]. For certain pairs of frequencies this difference can be an even multiple of  $\pi$ , leading to almost identical phase behavior at two distinct frequencies. This opens up the possibility of having critical coupling at two distinct frequencies for large  $f$ . This is shown in Figures 3.5(c) (for TE) and in 3.5(d) (for TM) for  $d_1 = 70$  nm. We have plotted the intensity reflection coefficient as functions of wavelength. We have used slightly different sets of values for the two polarizations, namely, for TE (TM) we used  $d_2 = 85$  nm (98 nm). We again show the reflectivity profiles for the bare composite film on the substrate in Figures 3.5(a) and 3.5(b) for

reference. Curves 1, 2 and 3 for TE (TM) correspond to  $f$  values 0.01, 0.05 and 0.1 (0.01, 0.03 and 0.06). It is clear from Figures 3.5(c) and 3.5(d) that for low values of  $f \approx 0.01$ , one has only a single dip which breaks up into two with an increase in the oscillator strength. For optimal values of the volume fraction it is thus possible to have critical coupling at pairs of frequencies for both the polarizations.

### 3.4 Conclusions

In conclusion, we have studied critical coupling under oblique incidence and shown that almost all the incident energy can be absorbed in a metal-dielectric composite nano film for both TE and TM polarizations. The imprint of the bulk longitudinal plasmons can be seen in the scattering profiles for TM incidence, while the corresponding TE scattering does not show such features. For large oscillator strength of the Mie plasmons of the composite layer, critical coupling at dual frequencies for both TE and TM polarizations were shown to be feasible. Our structure excludes the excitation of surface modes at the composite-dielectric interfaces. It is clear that if the structure is loaded on top by a prism, or one of the surfaces is corrugated, the surface plasmons can be excited on the two interfaces of the composite film. It is of importance to study the critical coupling phenomenon in the presence of the surface excitations.

---

# 4 Photonic crystal waveguide interferometer with $\sim \lambda/1000$ fringe spacing

---

## 4.1 Introduction

The propagation of light through rectangular and planar multimode waveguides can result in interesting self-imaging effects based on multimode interference (MMI) phenomena [11, 51]. Over the last decade or so, these effects have been demonstrated as the basis of splitters (for example, [77]), modulators and switches [78], Mach-Zehnder interferometers [79], and laser resonators [2]. Optical waveguide interferometers have been used extensively as sensors for various applications. They are all based on the interference of the guided modes of the waveguide and have been used for chemical, biological and biochemical applications [80, 81]. They have also been used in devices as a modulator-switch [82].

Conventional interferometers like the Fabry-Pérot or the Michelson interferometers have a fringe spacing of  $\lambda/2$ . A new kind of waveguide interferometer was proposed by Ovchinnikov and Pfau [3] and reported to have a fringe spacing of  $\lambda/9$ . The implementation of the dual mode regime

for the operation of the interferometer was shown in [4] reporting a fringe spacing of  $\lambda/130$ .

In this chapter we propose the design of a planar waveguide interferometer that can have a fringe spacing of  $\sim \lambda/1000$  with photonic crystal walls. The analysis has been carried out using a second order accurate finite difference scheme for solving the scalar wave equation. This scheme makes no assumptions about having a paraxial input beam and can incorporate metals or dielectrics or a combination of both for the walls of the planar waveguide.

To present our work in the proper context, a brief review of the previous work is presented in the following section.

## 4.2 Previous work

### 4.2.1 The experiment of Ovchinnikov and Pfau (year 2001)

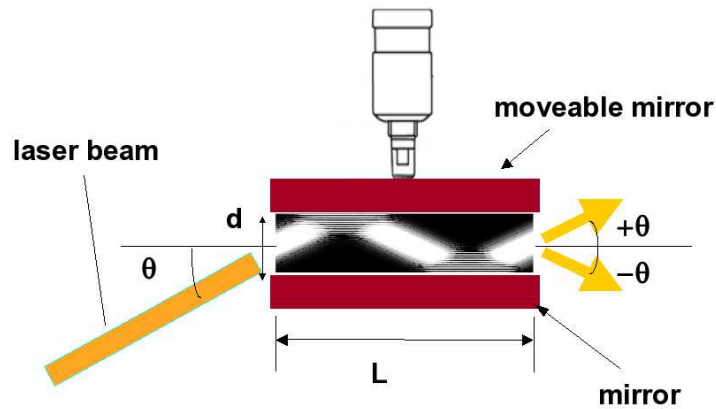


Figure 4.1: *Schematic diagram of the fiber coupled waveguide interferometer in [3]*

Ovchinnikov and Pfau [3] have described a novel form of multimode waveguide interferometer based on a planar waveguide formed from a pair of fully reflecting mirrors. As illustrated in Figure 4.1 the interferometer was composed of two fully reflecting mirrors. These formed a planar multimode waveguide. Light enters the waveguide at some angle  $+\theta$ . The magnitude of the angle is such that a spectrum of modes is excited. The ensuing multimode propagation results in oscillations and revivals in the transverse momentum of the propagating field [3]. This leads to the output beam swinging between angles of  $\pm \theta$  as the width of the waveguide was changed. In the experiments that Ovchinnikov and Pfau [3] performed, a 2.0 mm diameter beam from a  $0.633 \mu\text{m}$  source was coupled into a 50.0 mm long planar waveguide at an angle of 0.25 rad. Under this condition a 70.0 nm change in the  $30.0 \mu\text{m}$  guide width produced a complete cycle of the angular deviation of the output beam. The sensitivity to the change in guide width equates to a fringe spacing of  $\lambda/9$  [3].

Although this result is remarkable when compared with the  $\lambda/2$  displacement required in more conventional interferometers, the fringe spacing could, in principle, be even smaller if certain technical limitations could be overcome. This is what was achieved by Jenkins et. al.[4].

#### 4.2.2 The design of Jenkins et. al. (year 2008)

Following the suggestion of Ovchinnikov and Pfau [3], they repeated the experiment with a narrow waveguide containing only two propagating modes.

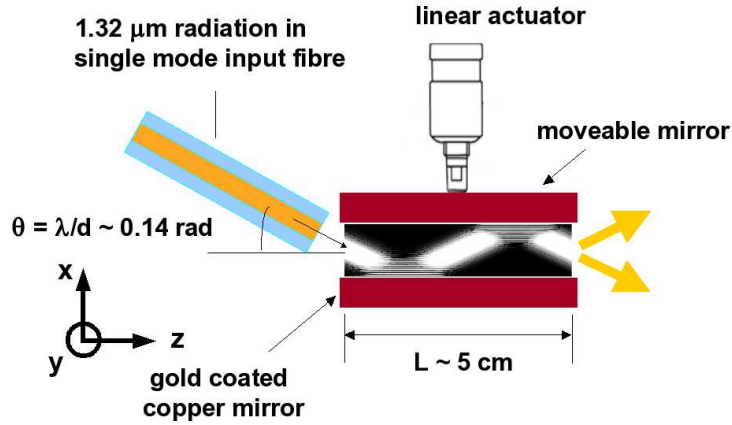


Figure 4.2: *Schematic diagram of the fiber coupled waveguide interferometer in [4]*

Additionally, they used a fiber for efficient coupling of light from the laser source into the waveguide. Finally, the laser source had a larger wavelength than what was used by Ovchinnikov and Pfau [3]. With these modifications, Jenkins et. al. were able to obtain a fringe spacing of  $\lambda/130$ , which is an order of magnitude better than previous results.

To implement the dual mode operational regime, the planar multimode waveguide was formed by two 50.0 mm diameter fully reflecting gold coated mirrors both having a surface figure of  $\lambda/10$  at 632.8 nm. One of the mirrors was held in a fixed precision mount, the other was mounted on a linear actuator. 1.32  $\mu\text{m}$  radiation from a Nd:YAG laser source was coupled to the planar waveguide from a single-mode, polarization maintaining fiber with an effective  $1/e^2$   $\text{TEM}_{00}$  mode diameter of 6.5  $\mu\text{m}$ . The fiber was held straight in a fiber guide and adjusted so that the polarization orientation of the output

field was parallel to the plane of the mirror surfaces, i.e., parallel to the  $y$  axis in Figure 4.2.

Initially the fiber axis was aligned to be colinear with the planar waveguide axis and butted up to it. Under this condition a choice of

$$d = 6.5\mu m / 0.703 = 9.25\mu m$$

maximizes the power coupling to its fundamental mode [83]. From this starting point, the fiber was tilted by an angle  $\theta$  with respect to the axis of the planar waveguide. In practice, although the last centimeter of the fiber was stripped back to its  $125\ \mu m$  cladding diameter, this still meant that the axis of the fiber pivoted about a  $62.5\ \mu m$  radius. Depending on the magnitude of  $\theta$ , this leads to a short free-space propagation distance and some diffraction before the beam enters the planar waveguide. This was taken into account in the overlap integral calculations to obtain the power coupling coefficients as a function of the input angle  $\theta$ .

As  $\theta$  increases, modes of higher order are excited in turn (see Figure 4.3). The peak in the excitation characteristic of any given higher order mode occurs when the angle of incidence of the input field corresponds to the angle of one of the plane wave components of the higher order mode itself. To a good approximation, to maximize the excitation of the  $TE_p$ -th mode, an input beam angle of  $\theta = \pm p\lambda/(2d)$  is required. Hence for  $p = 2$ , one obtains  $\theta = \pm\lambda/d = 1.32/9.25 = 0.14$  radian. As indicated in Figure 4.3, by choosing an input angle of half this magnitude, i.e.,  $\lambda/(2d) = 0.07$  radian, the excitation is essentially limited to two modes  $TE_1$  and  $TE_2$ .

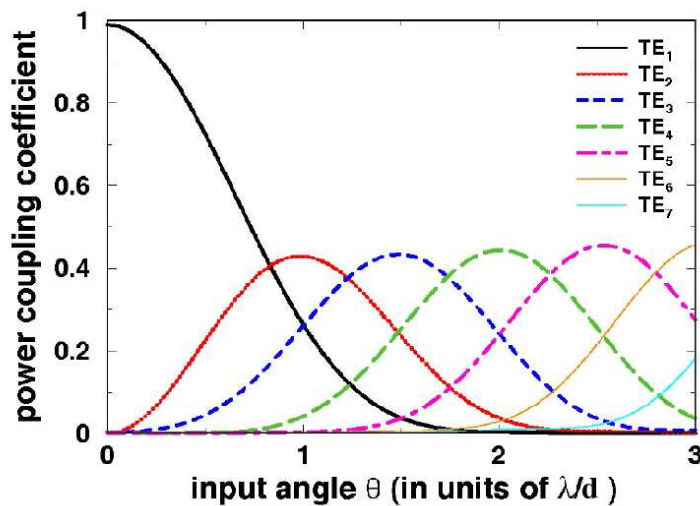


Figure 4.3: *Excitation of guided modes as a function of the input angle of the injected beam*[4]

With only the first two modes excited in the waveguide, the field profile in the input plane ( $z=0$ ) is given by:

$$E(x, 0) = c_1 E_1(x) + c_2 E_2(x) \quad (4.1)$$

where  $c_1$  and  $c_2$  are the coupling coefficients corresponding to the guided mode profiles  $E_1(x)$  and  $E_2(x)$  respectively.

The phase change between any two TE modes after propagation through an axial distance  $L$  is given by

$$\phi_{pq} = L(\beta_p - \beta_q) \quad (4.2)$$

where  $\beta_p$  is the phase coefficient of the  $TE_p$  mode:

$$\beta_p = \frac{2\pi}{\lambda} \left[ 1 - \left( \frac{p\lambda}{2d} \right)^2 \right]^{1/2} \quad (4.3)$$

Under the paraxial approximation, i.e.,

$$\beta_p \approx \frac{2\pi}{\lambda} \left[ 1 - \frac{1}{2} \left( \frac{p\lambda}{2d} \right)^2 \right] \quad (4.4)$$

the phase difference between two modes with indices  $p$  and  $q$  is given by:

$$\phi_{pq} = L \frac{\pi\lambda}{4d^2} (q^2 - p^2) \quad (4.5)$$

Putting  $p=1$  and  $q=2$ , we get

$$\phi_{12} = L \frac{3\pi\lambda}{4d^2} \quad (4.6)$$

Differentiating with respect to the guide width  $d$ , we obtain

$$\partial\phi_{12} = -L \frac{3\pi\lambda}{2d^3} \partial d \quad (4.7)$$

Equating Equation 4.7 to  $2\pi$  gives the incremental change in guide width that will produce a  $2\pi$  phase change between the modes, and hence, a change in the output beam angle from  $+\lambda/(2d)$  to  $-\lambda/(2d)$ , and back again, i.e. a fringe, as

$$\partial d = -\frac{4d^3}{3L\lambda} \quad (4.8)$$

Equation 4.8 suggests that small guide widths in conjunction with long waveguides and long wavelength radiation produce maximum sensitivity. However the attenuation of the modes at the guide walls will affect the power ratio between the modes and impact on the ability to measure variations in the output field due to incremental changes in the guide width.

The fractional power transmission for the mode  $TE_p$  through a planar waveguide of length  $L$  is given by

$$t_p = \exp(-2\alpha_p L)$$

$$\text{where, } \alpha_p = \frac{\lambda^2 p^2}{2d^3} \text{Re}[(\epsilon^2 - 1)^{1/2}] \quad (4.9)$$

is the attenuation coefficient. Here,  $\epsilon = n - ik$  is the complex refractive index of the wall material. With a  $1.32 \mu\text{m}$  source in conjunction with a  $50 \text{ mm}$  long planar waveguide formed from gold ( $n = 0.419$  and  $k = 8.42$ ) coated mirrors, Equation 4.9 yields the fractional power transmission as a function of mode number and guide width as,  $t_p = \exp(-503p^2/d^3)$ . For a guide width of  $7 \mu\text{m}$  this yields fractional transmission values for the modes  $TE_1$ ,  $TE_2$  and  $TE_3$  of 0.23, 0.003 and  $1.85 \times 10^{-6}$  respectively, with  $t_1/t_2 \sim 81$ . For a guide width of  $11 \mu\text{m}$ , the corresponding values are 0.68, 0.22 and 0.03, with  $t_1/t_2 \sim 3$ . From this perspective, with the aim of working with small guide widths in order to achieve high sensitivity, Jenkins et. al. opted for an input

angle of  $\pm\lambda/d$  (Figure 4.3) . This provided the highest starting magnitude of  $TE_2$ , while the additional excitation of the modes  $TE_3$  and  $TE_4$  were of little consequence because of their significantly higher attenuation (see Figure 4.4).

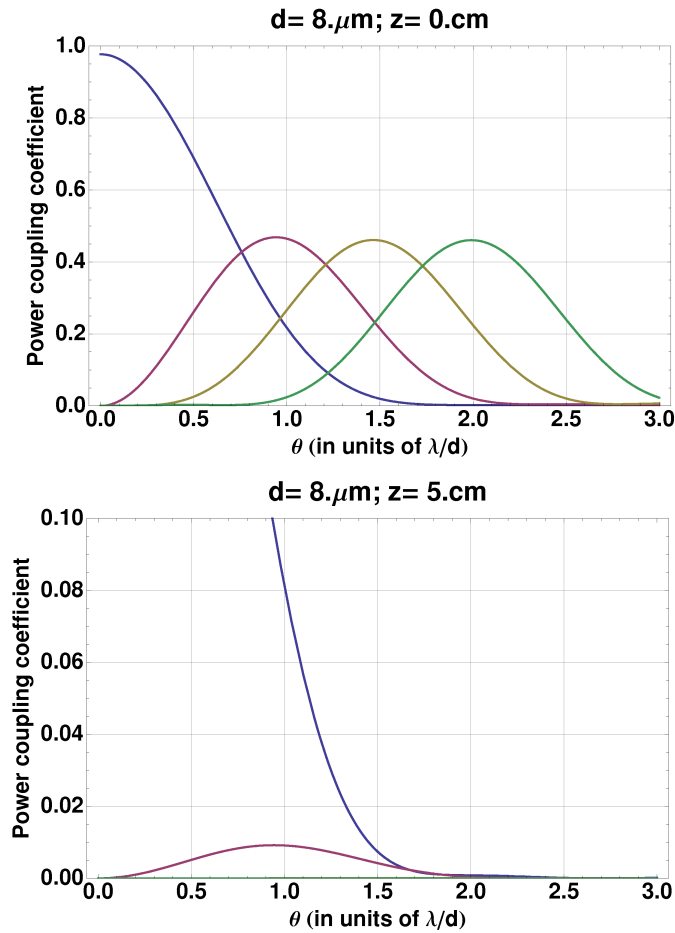


Figure 4.4: *The power coupling coefficient plots of a  $8\mu\text{m}$  wide waveguide with gold mirror walls at (top) the input plane ( $z=0$ ) and (bottom) the output plane ( $z=5\text{cm}$ ). Only insignificant amounts of the  $TE_3$  and  $TE_4$  modes survive at the guide exit.*

On the aforementioned basis, Jenkins et. al. started off with a guide width of  $11.0 \mu\text{m}$  and gradually reduced the width to  $8 \mu\text{m}$ . The launch angle  $\lambda/d$  was kept fixed at  $0.14$  radian corresponding to a median guide width of  $9.25 \mu\text{m}$ .

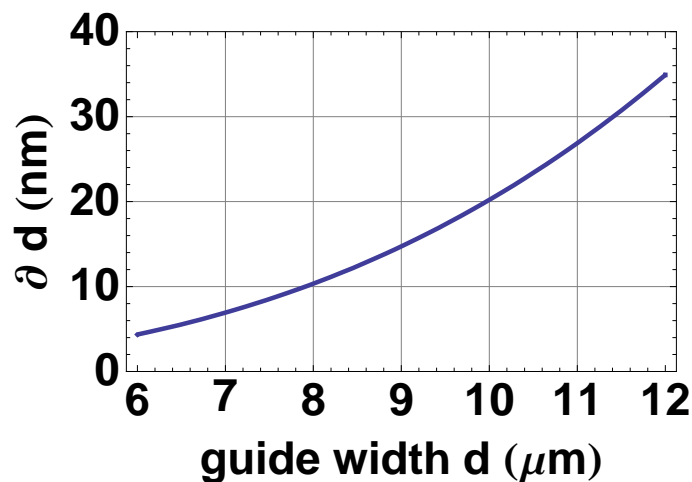


Figure 4.5: *The change in guide width required to produce a complete switching cycle of the beam at the output plane[4]. This plot is for  $L = 5\text{cm}$  and  $\lambda = 1.32\mu\text{m}$ .*

For each guide-width  $\partial d$  was measured very accurately. The measured values of  $\partial d$  were in very good agreement with the theoretical predictions plotted in Figure 4.5. In particular, it was observed that for  $d = 8\mu\text{m}$ ,  $L = 5\text{cm}$  and  $\lambda = 1.32\mu\text{m}$ ,  $\partial d \sim 10\text{nm} \simeq \lambda/130$  as predicted by Equation 4.8

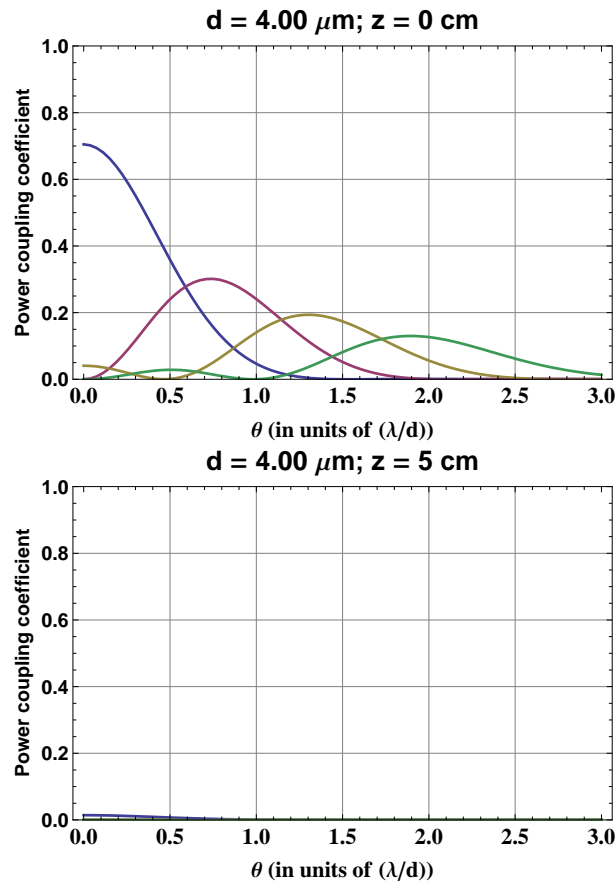


Figure 4.6: *The power coupling coefficient plots of a  $4\mu\text{m}$  wide waveguide with gold mirror walls at (top) the input plane ( $z=0$ ) and (bottom) the output plane ( $z=5\text{cm}$ )*

### 4.3 The present design

A guide with a smaller width seems to serve the purpose of making a more sensitive waveguide interferometer (see Figure 4.5 and Equation 4.8). However, the guide width cannot be reduced indefinitely as for small guide widths, attenuation of the higher order modes (see Equation 4.9) become prohibitive and only a small fraction of the modes, excited at the input plane, would survive at the output plane (for example see Figure 4.6). Thus, more sensitive

waveguide interferometers can be achieved only if the loss at the walls can be reduced.

Photonic band gap structures are strong candidates for making waveguides owing to many features like lossless nature of propagation and scalability of the design. One-dimensional photonic band gap structures are the easier to fabricate with well accepted methods compared to the higher dimensional counterparts [84, 85, 86]. The use of lossless materials like photonic crystals would allow us to use smaller guide widths in order to achieve a sensitive interferometer.

Thus we study a waveguide interferometer system which is the same as in [4] except for the walls where we have used finite-sized one-dimensional photonic crystals. All the other parameters, namely, the wavelength, waist size of the input beam and the propagation distance for obtaining the two-mode interference pattern are chosen the same for ease of comparison.

## 4.4 Method used

A two mode interference pattern at the exit plane of the waveguide requires the calculation of the propagation constants and the mode profiles of the guided modes. In what follows, the second order accurate finite difference scheme for obtaining the propagation constants of the modes and extraction of the guided modes are described. The coupling of the input Gaussian beam into the waveguide and the choice of a proper tilt angle so as to obtain a two mode interference at the output plane is explained. The results are validated

by comparison with those of [4] in the following section.

#### 4.4.1 Determining the propagation constants

A non-iterative finite difference scheme has been used for evaluating the propagation constants of the waveguide. The wave equation

$$\frac{d^2 E(x)}{dx^2} + k_0^2 \epsilon(x) E(x) = \beta^2 E(x) \quad (4.10)$$

where  $k_0 = 2\pi/\lambda_0$ ,  $\lambda_0$  is the free space wavelength is discretized in accordance with the second order accurate finite difference scheme as:

$$\frac{E_{i-1} - 2E_i + E_{i+1}}{\delta^2} + k_i^2 E_i = \beta^2 E_i \text{ for all } i \in I \quad (4.11)$$

where

$\delta =$  distance between two neighbouring grid points

$$k_i^2 \equiv k(x_i)^2 = k_0^2 \epsilon(x_i),$$

$\epsilon(x_i)$  is the dielectric constant at the point  $x_i$

$$E_i \equiv E(x_i)$$

A finite domain for the dielectric distribution is chosen and Equation 4.11 at each  $x_i$  is written. The whole set of equations thus obtained along with the boundary condition that  $E_i$  at the ends of the computational domain is zero gives an eigenvalue system. Writing down Equation 4.11 for all the values  $1 < i < N$  and casting them in matrix form, we get the following

matrix equation:

$$\begin{pmatrix}
 k_1^2 - \frac{2}{\delta^2} & \frac{1}{\delta^2} & 0 & 0 & \cdots & 0 \\
 \frac{1}{\delta^2} & k_2^2 - \frac{2}{\delta^2} & \frac{1}{\delta^2} & 0 & \cdots & \vdots \\
 0 & \frac{1}{\delta^2} & k_3^2 - \frac{2}{\delta^2} & \frac{1}{\delta^2} & \cdots & \vdots \\
 \vdots & & & \ddots & & \vdots \\
 \vdots & & & & \ddots & \frac{1}{\delta^2} \\
 0 & & \cdots & 0 & \frac{1}{\delta^2} & k_N^2 - \frac{2}{\delta^2}
 \end{pmatrix}
 \begin{pmatrix}
 E_1 \\
 E_2 \\
 E_3 \\
 \vdots \\
 \vdots \\
 E_N
 \end{pmatrix}
 = \beta^2
 \begin{pmatrix}
 E_1 \\
 E_2 \\
 E_3 \\
 \vdots \\
 \vdots \\
 E_N
 \end{pmatrix}
 \tag{4.12}$$

The eigenvalues are the squares of the propagation constants and the eigenvectors are the field distributions. We use this scheme because it evaluates the propagation constants non-iteratively as opposed to the iterative schemes used previously (see for example [87]). Moreover when using metals, the guided modes have an imaginary part corresponding to the loss associated with the metallic boundaries. Calculating complex propagation constants using iterative schemes require root finding algorithms to search over a very large domain of values that cannot be guessed reasonably. The trade-off for a quick search of the propagation constants is the diagonalization of a large (1500x1500 or larger, depending on the waveguide structure) tridiagonal matrix for a finely subdivided domain of the dielectric distribution.

#### 4.4.2 Extraction of the guided modes

The solutions also include other modes that satisfy the same boundary conditions. We use the following constraints[88, 89] to retrieve the guided modes from the whole set of solutions:

If the dielectric distribution contains absorptive materials.

$$\text{Re}(n_{cladding}) < \text{Re}\left(\frac{\beta}{k_0}\right) < \text{Re}(n_{core}) \quad (4.13)$$

The constraint when pure dielectrics are used is

$$\text{Re}\left(\frac{\beta}{k_0}\right) < \text{Re}(n_{core}) \text{ and } \text{Im}\left(\frac{\beta}{k_0}\right) = 0 \quad (4.14)$$

where  $n_{core}$  and  $n_{cladding}$  are the refractive indices of the core and cladding material.

An input beam can be expressed in terms of the guided modes as :

$$E(x, z) = \sum_m c_m E_m(x) e^{-i\beta_m z} \quad (4.15)$$

The coupling coefficients of the guided modes ( $c_m$ ) are a function of the input angle of the beam. For a tilted Gaussian input beam they are given by

$$c_m(\theta) = \int_{x_1}^{x_N} E(x'', z'') E_m^*(x) dx \quad (4.16)$$

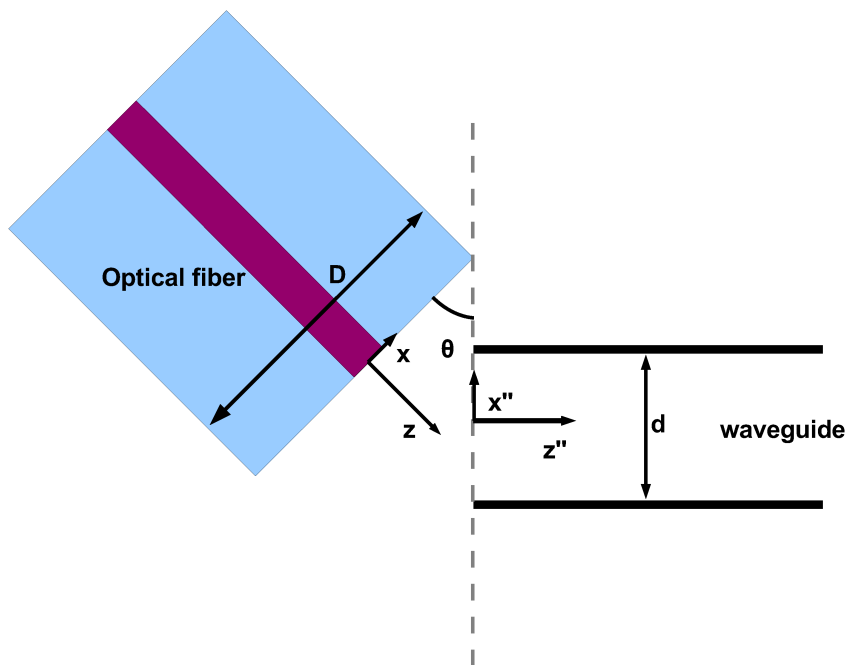


Figure 4.7: Transformation of coordinates for the tilted beam injected into the waveguide.

Here  $x_1$  and  $x_N$  are the limits of the dielectric distribution,  $E_m(x)$  is the  $m$ -th guided mode profile and  $E(x, z)$  is the input beam profile given by:

$$E(x, z) = \sqrt[4]{\frac{2}{\pi}} \frac{e^{i\phi(z)/2}}{\sqrt{w(z)}} \exp \left[ -ik_0 z - \frac{ik_0 x^2}{2R(z)} - \frac{x^2}{w^2(z)} \right]$$

$$\phi(z) = \tan^{-1}(z/z_R)$$

$$w(z) = w_0(\sqrt{1 + (z/z_R)^2})$$

$$R(z) = (z + z_R^2/z)$$

(4.17)

The following transformations are made for a tilt  $\theta$

$$\begin{aligned}x'' &= x \cos \theta \\z'' &= x \sin \theta + (D/2) \tan \theta\end{aligned}\tag{4.18}$$

$D$  being the diameter of the fiber delivering the input (See Figure 4.7).

## 4.5 Results

We compare the values of the attenuation constants for the case in [4] by this method with that of the analytical expression as a test of the reliability of this method in Figure 4.8.

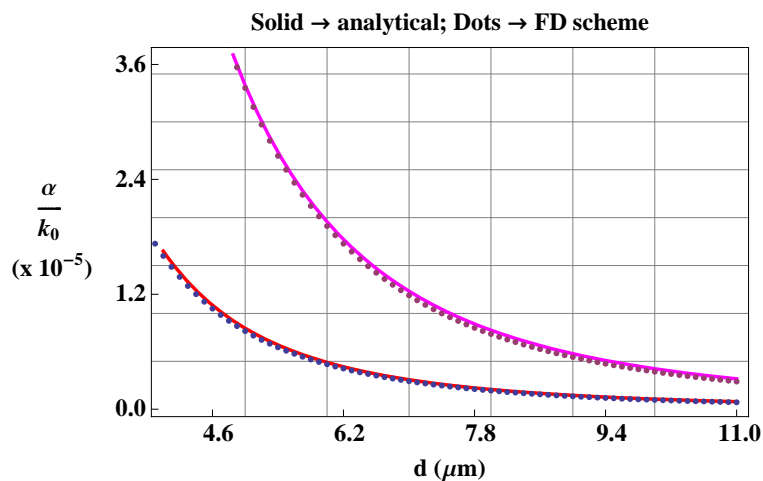


Figure 4.8: Attenuation constants corresponding to the first two modes using analytical formula (solid lines) and the finite difference scheme (dots) for the system in [4].

In Figure 4.9 we show the coupling coefficients of the same system as in

[4].

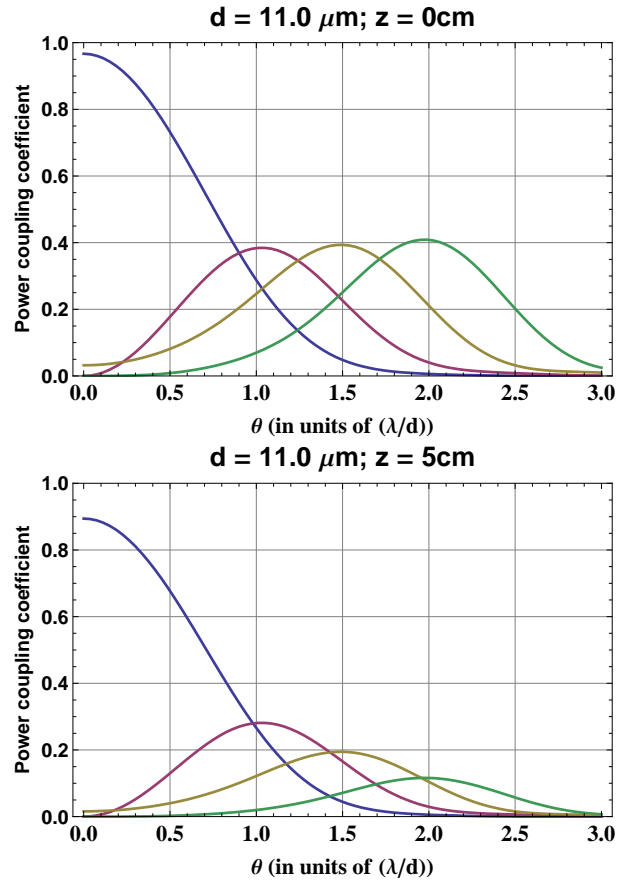


Figure 4.9: The power coupling coefficient plots of a  $11\mu\text{m}$  wide waveguide with gold mirror walls at (top) the input plane ( $z=0$ ) and (bottom) the output plane ( $z=5\text{cm}$ )

Next, we note that for a finite sized one dimensional photonic crystal consisting of slabs of  $\lambda/4$  plates of two materials placed alternately, not more than 10 pairs of slabs shall be necessary to reflect the beam back completely into the waveguide core(for example [48]).

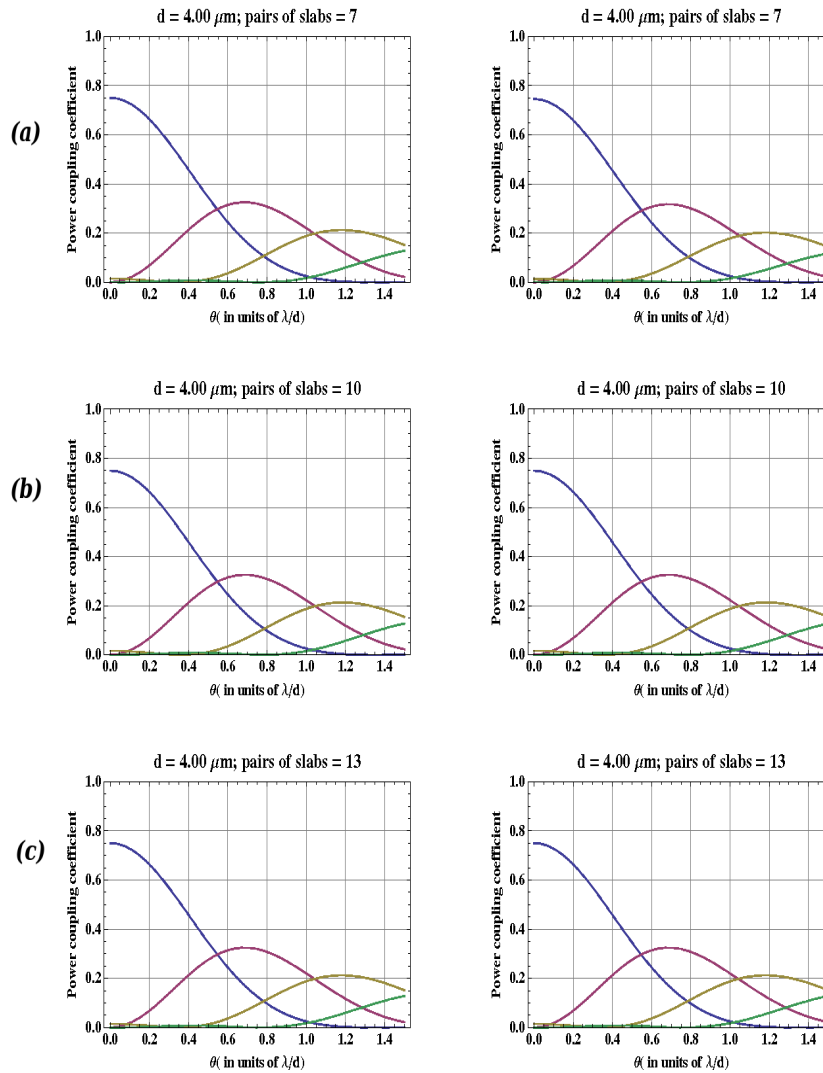


Figure 4.10: Plot of the power coupling coefficient vs input angle of the beam for various thickness of the finite photonic crystal walls at a guide width of  $4\mu\text{m}$ . The left column is the profile at the input plane ( $z=0$ ). The plots on the right side are the power coupling coefficients at the exit plane ( $z=5\text{cm}$ ). The cladding beyond the photonic crystal layers are of absorbing material (Ge). There is a slight attenuation with 7 pairs of slabs (a). There is no change of the power coupling coefficient profile if 10 or more layers (b) and (c) respectively) are used.

In Figure 4.10 we plot the power coupling coefficient as a function of the input angle ( $\theta$ ) for planar waveguides with photonic crystal walls differing in the number of slabs used. The walls consist of a finite number of  $\lambda/4$  plates and an absorbing material (like Ge) beyond. There is no change of the power coupling coefficient profile for photonic crystal slabs with 10 or more pairs of slabs. We therefore use 10 pairs of slabs in our calculations. If such a large number of slabs are used, the material surrounding the cladding does not affect the field profiles. The lossless nature of the photonic crystal waveguide is seen from the power coupling coefficient plots at the input and the output planes.

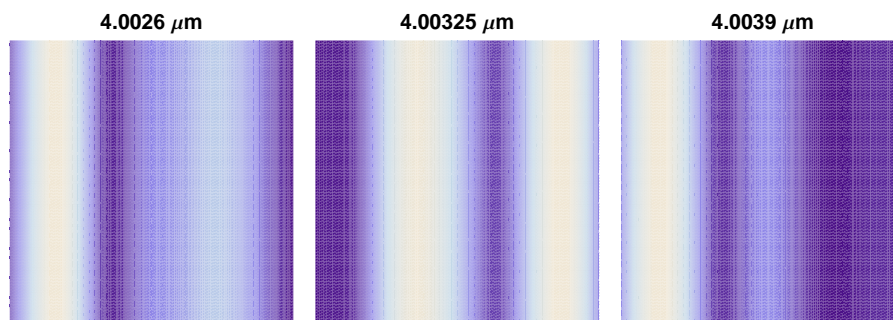


Figure 4.11: *The contour plots of the electric field intensities at the exit plane for different guide widths. The values of the guide widths are given above the figures.*

We show the field profile at the exit end for slight change in the guide width in Figure 4.11. This amounts to a shift in the fringe pattern for a change in the guide width of 1.3nm for a guide width of  $4\mu\text{m}$ . Such small changes in guide width are detectable due to the lossless nature of the

dielectric walls and the mode coupling that still occurs at such small guide widths.

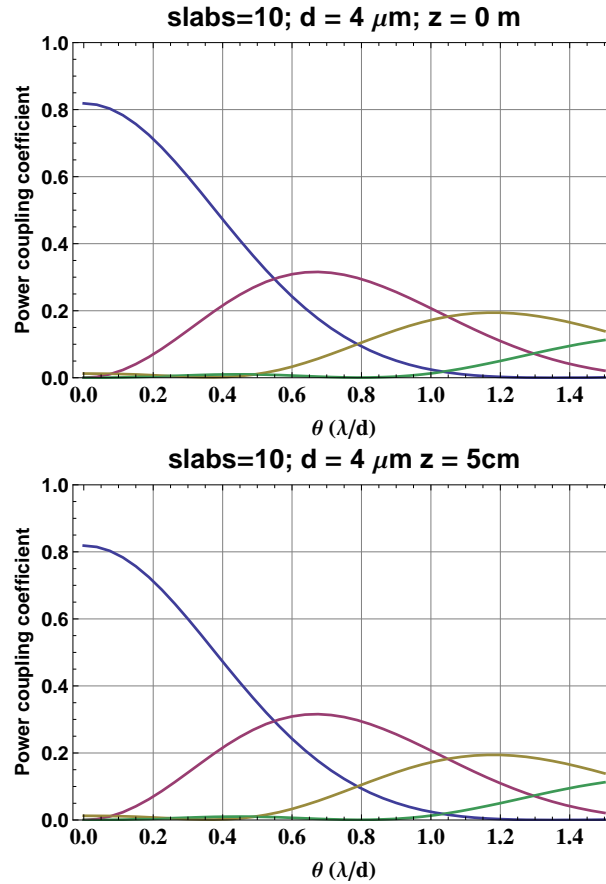


Figure 4.12: *The power coupling coefficient plots of a 4μm wide waveguide with photonic crystal walls at (left) the input plane ( $z=0$ ) and (right) the output plane ( $z=5\text{cm}$ )*

A waveguide with such photonic crystal walls was studied using a finite difference scheme [87, 90] for the fringe displacement sensitivity. The tilt angle for the input beam was chosen to be  $\theta = 0.5$  (in units of  $\lambda/d$ ) so that the first two modes produce an interference fringe at the output plane (Figure

4.12). There was no loss of the modes for transmission over a length of 5cm. This and the strong coupling of the modes even at small guide widths of  $4\mu m$  improved the fringe displacement sensitivity.

At  $\lambda = 1.32\mu m$ , the change in guide-width necessary to produce a complete switching cycle of the fringe pattern (Figure 4.11) is  $1.3nm (\approx \lambda/1000)$ .

## 4.6 Conclusion

In conclusion, we have shown that a waveguide interferometer with photonic crystal walls with a guide-width sensitivity of  $\sim \lambda/1000$  can be achieved. The ability to go to guide widths as small as  $\sim 4\mu m$  was not possible earlier with metal-walled waveguides due to severe attenuation of all the guided modes. Moreover, such a sensitive interferometer can be designed for various wavelengths owing to the scalability of the photonic crystal structures.

---

## 5 Conclusion and future prospects

---

In this thesis, we have presented the design of a dual case I self-imaging waveguide resonator with variable reflectivity mirrors, a critical coupling resonator dealing with oblique incidence and an ultra-sensitive waveguide interferometer using photonic crystal structure for the walls.

In Chapter 2 a novel class of a waveguide resonator based on self-imaging has been proposed. The self-imaging length depends on the guide-width and the wavelength of the electromagnetic radiation used. The longitudinal and transverse distances have been scaled in units of the self-imaging length and the guide-half width respectively. This provides a generalized resonator design for an arbitrary wavelength. Moreover, the dual Case I design requires only plane mirrors with step-index reflectivity profiles to be placed at the ends of the waveguide. Such mirrors are easier to produce and install as compared to their curved mirror counterparts. The resonator can even be fabricated in semiconductor integrated optics technology where cleaved facets can act as plane mirrors.

In Chapter 3 a critically coupled resonator has been studied in detail. Earlier studies of the system dealt with the case of normal incidence showing

critical coupling at one or two frequencies. The distinguishability of the transverse electric and transverse magnetic polarizations for oblique incidence (as opposed to the case of normal incidence) has been dealt with in this study. It has been shown that critical coupling can be achieved for both the polarizations, although at different frequencies. The signatures of bulk plasmons that can only be excited by the transverse magnetically polarized component of the incident radiation have also been found.

In Chapter 4 an ultra-sensitive waveguide interferometer using photonic crystal structure for the walls has been studied. This is an order of magnitude improvement on the sensitivity of a recently proposed design of a metal-clad waveguide interferometer. This photonic crystal waveguide structure allows us to go to smaller guide widths that could not be attained previously with metal waveguides.

Analysis of similar systems can be carried out with higher dimensional photonic band gap structures since prohibition of electromagnetic wave propagation along two directions is expected to yield different field profiles than has been observed in this work.

---

## Bibliography

---

- [1] J. Pendry and A. MacKinnon, “Calculation of photon dispersion relations,” *Physical Review Letters*, vol. 69, no. 19, pp. 2772–2775, 1992.
- [2] J. Banerji, A. Davies, and R. Jenkins, “Laser resonators with self-imaging waveguides,” *Journal of the Optical Society of America B*, vol. 14, no. 9, pp. 2378–2380, 1997.
- [3] Y. B. Ovchinnikov and T. Pfau, “Revivals and oscillations of the momentum of light in a planar multimode waveguide,” *Physical Review Letters*, vol. 87, p. 123901, Aug 2001.
- [4] R. Jenkins, A. Blockley, J. Banerji, and A. Davies, “Fiber-coupled dual-mode waveguide interferometer with  $\lambda/130$  fringe spacing,” *Physical Review Letters*, vol. 100, no. 16, p. 163901, 2008.
- [5] J. Joannopoulos, P. Villeneuve, and S. Fan, “Photonic crystals: putting a new twist on light,” *Nature*, vol. 386, no. 6621, pp. 143–149, 1997.
- [6] E. Yablonovitch, “Photonic Crystals: Semiconductors of Light,” *Scientific American*, p. 47, December, 2001.

- [7] D. Angelakis, P. Knight, and E. Paspalakis, “Photonic crystals and inhibition of spontaneous emission: an introduction,” *Contemporary Physics*, vol. 45, no. 4, pp. 303–318, 2004.
- [8] J. Pendry, “Photonic band gap materials,” *Current Science*, vol. 76, no. 10, pp. 1311–1316, 1999.
- [9] H. Talbot, “Facts related to optical science,” *Philosophical Magazine*, vol. 9, pp. 401–407, 1836.
- [10] K. Patroski, “The self-imaging phenomenon and its applications,” *Progress in Optics*, vol. 27, pp. 1–108, 1989.
- [11] O. Bryngdahl, “Image formation using self-imaging techniques,” *Journal of the Optical Society of America*, vol. 63, pp. 416–419, 1973.
- [12] J. Degnan and D. Hall, “Finite-aperture waveguide-laser resonators,” *Quantum Electronics, IEEE Journal of*, vol. QE-9, pp. 901–910, 1973.
- [13] J. Rayleigh, “On the remarkable phenomenon of crystalline reflexion described by Prof. Stokes,” *Philosophical Magazine*, vol. 26, pp. 256–265, 1888.
- [14] E. Yablonovitch, “Inhibited Spontaneous Emission in Solid-State Physics and Electronics,” *Physical Review Letters*, vol. 58, no. 20, pp. 2059–2062, 1987.

- [15] S. John, “Strong localization of photons in certain disordered dielectric superlattices,” *Physical Review Letters*, vol. 58, no. 23, pp. 2486–2489, 1987.
- [16] E. Yablonovitch, “Photonic band-gap crystals,” *Journal of Physics: Condensed Matter*, vol. 5, pp. 2443–2460, 1993.
- [17] K. Ho, C. Chan, and C. Soukoulis, “Existence of a photonic gap in periodic dielectric structures,” *Physical Review Letters*, vol. 65, no. 25, pp. 3152–3155, 1990.
- [18] J. Joannopoulos, R. Meade, and J. Winn, *Photonic Crystals: Molding the Flow of Light*. Princeton University Press, 1995.
- [19] A. Chutinan and S. Noda, “Effects of structural fluctuations on the photonic bandgap during fabrication of a photonic crystal: a study of a photonic crystal with a finite number of periods,” *Journal of the Optical Society of America B*, vol. 16, no. 9, pp. 1398–1402, 1999.
- [20] M. De Dood, E. Snoeks, A. Moroz, and A. Polman, “Design and optimization of 2D photonic crystal waveguides based on silicon,” *Optical and Quantum Electronics*, vol. 34, no. 1, pp. 145–159, 2002.
- [21] J. Smajic, C. Hafner, and D. Erni, “Automatic calculation of band diagrams of photonic crystals using multiple multipole method,” *Applied Computational Electromagnetics Society Journal*, vol. 19, no. 1a, pp. 46–54, 2004.

- [22] K. Leung, “Defect modes in photonic band structures: a Green’s function approach using vector Wannier functions,” *Journal of the Optical Society of America B*, vol. 10, pp. 303–303, 1993.
- [23] A. Taflove and S. Hagness, *Computational electrodynamics: the finite-difference time-domain method*. Artech House, Boston, 1995.
- [24] D. Hermann, M. Frank, K. Busch, and P. Wolfe, “Photonic band structure computations,” *Optics Express*, vol. 8, no. 3, pp. 167–172, 2001.
- [25] W. Zhi, R. Guobin, L. Shuqin, and L. Weijun, “Compact supercell method based on opposite parity for Bragg fibers,” *Optics Express*, vol. 26, pp. 3542–3549, December 2003.
- [26] S. Jun, Y. Cho, and S. Im, “Moving least-square method for the band-structure calculation of 2D photonic crystals,” *Optics Express*, vol. 11, no. 6, pp. 541–551, 2003.
- [27] M. Dems, R. Kotynski, and K. Panajotov, “Plane Wave Admittance Method - a novel approach for determining the electromagnetic modes in photonic structures,” *Optics Express*, vol. 13, no. 9, pp. 3196–3207, 2005.
- [28] Z. Zhu and T. Brown, “Full-vectorial finite-difference analysis of microstructured optical fibers,” *Optics Express*, vol. 10, no. 17, pp. 853–864, 2002.

- [29] D. Chigrin, A. Lavrinenko, and C. Torres, “Nanopillars photonic crystal waveguides,” *Optics Express*, vol. 12, pp. 617–622, February 2004.
- [30] A. Martínez and J. Martí, “Analysis of wave focusing inside a negative-index photonic-crystal slab,” *Optics Express*, vol. 13, no. 8, pp. 2858–2868, 2005.
- [31] C. Neff and C. Summers, “A photonic crystal superlattice based on triangular lattice,” *Optics Express*, vol. 13, no. 8, pp. 3166–3173, 2005.
- [32] W. Saj, “FDTD simulations of 2D plasmon waveguide on silver nanorods in hexagonal lattice,” *Optics Express*, vol. 13, no. 13, pp. 4818–4827, 2005.
- [33] Z. Tang, R. Peng, D. Fan, S. Wen, H. Zhang, and L. Qian, “Absolute left-handed behaviors in a triangular elliptical-rod photonic crystal,” *Optics Express*, vol. 13, no. 24, pp. 9796–9803, 2005.
- [34] H. Kurt and D. Citrin, “Annular photonic crystals,” *Optics Express*, vol. 13, no. 25, pp. 10316–10326, 2005.
- [35] H. Kim, I. Park, B. O, S. Park, E. Lee, and S. Lee, “Self-imaging phenomena in multi-mode photonic crystal line-defect waveguides: application to wavelength de-multiplexing,” *Optics Express*, vol. 12, no. 23, pp. 5625–5633, 2004.
- [36] Y. Hsue and T. Yang, “Applying a modified plane-wave expansion method to the calculations of transmittivity and reflectivity of a semi-

- infinite photonic crystal,” *Physical Review E*, vol. 70, no. 1, p. 016706, 2004.
- [37] K. Busch, G. von Freymann, S. Linden, S. Mingaleev, L. Tkeshelashvili, and M. Wegener, “Periodic nanostructures for photonics,” *Physics Reports*, vol. 444, no. 3-6, pp. 101–202, 2007.
- [38] D. Cassagne, C. Jouanin, and D. Bertho, “Hexagonal photonic-band-gap structures,” *Physical Review B*, vol. 53, no. 11, pp. 7134–7142, 1996.
- [39] Z. Li and K. Ho, “Light propagation in semi-infinite photonic crystals and related waveguide structures,” *Physical Review B*, vol. 68, no. 15, p. 155101, 2003.
- [40] J. Arriaga, J. Knight, and P. Russell, “Modeling the propagation of light in photonic crystal fibers,” *Physica D: Nonlinear Phenomena*, vol. 189, no. 1-2, pp. 100–106, 2004.
- [41] A. Birner, R. Wehrspohn, U. Göesele, and K. Busch, “Silicon-Based Photonic Crystals,” *Advanced Materials*, vol. 13, no. 6, pp. 377–388, 2001.
- [42] M. Leutenegger, I. Utke, O. Martin, and P. Hoffmann, “Computation of custom made photonic crystals,” tech. rep., Swiss Federal Institute of Technology Lausanne, 2002.

- [43] J. Arriaga, A. Ward, and J. Pendry, “Order-N photonic band structures for metals and other dispersive materials,” *Physical Review B*, vol. 59, no. 3, pp. 1874–1877, 1999.
- [44] A. Ward and J. Pendry, “Refraction and geometry in Maxwell’s equations,” *Journal of Modern Optics*, vol. 43, no. 4, pp. 773–793, 1996.
- [45] J. Pendry, *Low Energy Electron Diffraction*. Academic Press, London, 1974.
- [46] P. Yeh, *Optical waves in layered media*. Wiley New York, 1988.
- [47] M. Born and E. Wolf, *Principles of optics*. Cambridge University Press, 1999.
- [48] D. Griffiths and C. Steinke, “Waves in locally periodic media,” *American Journal of Physics*, vol. 69, p. 137, 2001.
- [49] H. Benisty and C. Weisbuch, “Photonic crystals,” *Progress in Optics*, vol. 49, pp. 177–313, 2006.
- [50] L. Rivlin and V. Shul’Dyaev, “Multimode waveguides for coherent light,” *Izv. Vyssh. Uchebn. Zaved. Radiofiz.*, vol. 11, pp. 572–578, 1968.
- [51] R. Ulrich and G. Ankele, “Self-imaging in homogeneous planar optical waveguides,” *Applied Physics Letters*, vol. 27, pp. 337–339, 1975.
- [52] J. Banerji, A. Davies, C. Hill, R. Jenkins, and J. Redding, “Effects of curved mirrors in waveguide resonators,” *Applied Optics*, vol. 34, no. 16, pp. 3000–3008, 1995.

- [53] D. Henderson, “Waveguide lasers with intracavity electrooptic modulators: misalignment loss,” *Applied Optics*, vol. 15, pp. 1066–1070, 1976.
- [54] A. Fox and T. Li, “Resonant modes in a maser interferometer,” *Bell System Technical Journal*, vol. 40, pp. 453–488, 1961.
- [55] M. G. J.C., “Colours in Metal Glasses and in Metallic Films,” *Philosophical Transactions of the Royal Society of London. Series A*, vol. 203, 1904.
- [56] B. C.F. and H. D.R., *Absorption and scattering of light by small particles*. New York:John Wiley and Sons, 1983.
- [57] S. Dutta Gupta, “Nonlinear optics of stratified media,” *Progress in Optics*, vol. 38, pp. 1–84, 1998.
- [58] C. Nan, “Physics of inhomogeneous inorganic materials,” *Progress in Materials Science*, vol. 37, no. 1, pp. 1–116, 1993.
- [59] G. Agarwal and S. Dutta Gupta, “T-matrix approach to the nonlinear susceptibilities of heterogeneous media,” *Physical Review A*, vol. 38, no. 11, pp. 5678–5687, 1988.
- [60] G. Fischer, R. Boyd, R. Gehr, S. Jenekhe, J. Osaheni, J. Sipe, and L. Weller-Brophy, “Enhanced Nonlinear Optical Response of Composite Materials,” *Physical Review Letters*, vol. 74, no. 10, pp. 1871–1874, 1995.
- [61] G. Niklasson, “Modeling the optical properties of nanoparticles,” *SPIE Newsroom*.

- [62] C. Sönnichsen, T. Franzl, T. Wilk, G. Plessen, and J. Feldmann, “Plasmon resonances in large noble-metal clusters,” *New Journal of Physics*, vol. 4, no. 93.1, 2002.
- [63] M. Kulkarni, N. Seshadri, V. Rao, and S. Gupta, “Control of superluminal transit through a heterogeneous medium,” *Journal of Modern Optics*, vol. 51, no. 4, pp. 549–557, 2004.
- [64] S. Porel, S. Singh, S. Harsha, D. Narayana Rao, and T. Radhakrishnan, “Nanoparticle-embedded polymer: In situ synthesis, free-standing films with highly monodisperse silver nanoparticles and optical limiting,” *Chemistry of materials*, vol. 17, no. 1, pp. 9–12, 2005.
- [65] N. Halas, “The Optical Properties of Nanoshells,” *Optics and Photonics News*, vol. 13, no. 8, pp. 26–30, 2002.
- [66] J. West and N. Halas, “Engineered nanomaterials for biophotonics applications: Improving sensing, imaging, and therapeutics,” *Annual Review of Biomedical Engineering*, vol. 5, no. 1, pp. 285–292, 2003.
- [67] S. Dutta Gupta, “Strong-interaction mediated critical coupling at two distinct frequencies,” *Optics Letters*, vol. 32, no. 11, pp. 1483–1485, 2007.
- [68] J. Tischler, M. Bradley, and V. Bulovic, “Critically coupled resonators in vertical geometry using a planar mirror and a 5 nm thick absorbing film,” *Optics Letters*, vol. 31, no. 13, pp. 2045–2047, 2006.

- [69] J. Tischler, M. Scott Bradley, Q. Zhang, T. Atay, A. Nurmikko, and V. Bulović, “Solid state cavity QED: Strong coupling in organic thin films,” *Organic Electronics*, vol. 8, no. 2-3, pp. 94–113, 2007.
- [70] M. Hutley and D. Maystre, “The total absorption of light by a diffraction grating,” *Optics Communications*, vol. 19, no. 3, pp. 431–436, 1976.
- [71] L. Mashev, E. Popov, and E. Loewen, “Brewster effects for deep metallic gratings,” *Applied Optics*, vol. 28, pp. 2538–2541, 1989.
- [72] P. Johnson and R. Christy, “Optical Constants of the Noble Metals,” *Physical Review B*, vol. 6, no. 12, pp. 4370–4379, 1972.
- [73] U. Kreibig, “Electronic properties of small silver particles: the optical constants and their temperature dependence,” *Journal of Physics F: Metal Physics*, vol. 4, pp. 999–1014, 1974.
- [74] G. Agarwal and S. Dutta Gupta, “Interaction between surface plasmons and localized plasmons,” *Physical Review B*, vol. 32, no. 6, pp. 3607–3611, 1985.
- [75] P. Rouard and A. Meessen, “Optical Properties of Thin Metal Films,” *Progress in Optics*, vol. 31, pp. 77–77, 1993.
- [76] E. Burstein, *Elementary excitations in solids*. New York: Plenum Press, 1969.

- [77] R. Jenkins, R. Devereux, and J. Heaton, "Waveguide beam splitters and recombiners based on multimode propagation phenomena," *Optics Letters*, vol. 17, no. 14, pp. 991–993, 1992.
- [78] R. Jenkins, J. Heaton, D. Wight, J. Parker, J. Birbeck, G. Smith, and K. Hilton, "Novel  $1 \times N$  and  $N \times N$  integrated optical switches using self-imaging multimode GaAs/AlGaAs waveguides," *Applied Physics Letters*, vol. 64, p. 684, 1994.
- [79] R. Jenkins, R. Devereux, and J. Heaton, "Novel waveguide Mach-Zehnder interferometer based on multimode interference phenomena," *Optics Communications*, vol. 110, p. 410, 1994.
- [80] Z. Qi, K. Itoh, M. Murabayashi, and H. Yanagi, "A composite optical waveguide-based polarimetric interferometer for chemical and biological sensing applications," *Journal of Lightwave Technology*, vol. 18, no. 8, pp. 1106–1110, 2000.
- [81] B. Shew, C. Kuo, Y. Huang, and Y. Tsai, "UV-LIGA interferometer biosensor based on the SU-8 optical waveguide," *Sensors & Actuators A: Physical*, vol. 120, no. 2, pp. 383–389, 2005.
- [82] W. Martin, "Optical waveguide interferometer modulator-switch," Jan. 24 1978. US Patent 4,070,094.

- [83] D. Henderson, “Waveguide lasers with intracavity electrooptic modulators- Misalignment loss,” *Applied Optics*, vol. 15, pp. 1066–1070, 1976.
- [84] C. Soukoulis, “The history and a review of the modelling and fabrication of photonic crystals,” *Nanotechnology*, vol. 13, no. 3, pp. 420–423, 2002.
- [85] S. Corzine, M. Tan, C. Lin, J. Zhu, and M. Leary, “Distributed bragg reflector and method of fabrication, <http://www.freepatentsonline.com/20060285211.html>,” December 2006.
- [86] S. Akiyama, F. Grawert, J. Liu, K. Wada, G. Celler, L. Kimerling, and F. Kaertner, “Fabrication of highly reflecting epitaxy-ready Si-SiO<sub>2</sub> Bragg reflectors,” *Photonics Technology Letters, IEEE*, vol. 17, no. 7, pp. 1456–1458, 2005.
- [87] D. Heatley, G. Vitrant, and A. Kevorkian, “Simple finite-difference algorithm for calculating waveguide modes,” *Optical and Quantum Electronics*, vol. 26, no. 3, pp. 151–163, 1994.
- [88] H. Uranus, *Guiding light by and beyond the total internal reflection mechanism*. PhD thesis, University of Twente, Enschede, The Netherlands, April 2004.

- [89] P. Bienstman, *Rigorous and efficient modelling of wavelength scale photonic components*. PhD thesis, Ghent University, Department of Information Technology, May 2001.
- [90] K. Kawano and T. Kitoh, *Introduction to optical waveguide analysis*. Wiley Chichester, 2001.

## List of publications

1. "Critical coupling at oblique incidence", Subimal Deb , Shourya Dutta Gupta , J. Banerji and S. Dutta Gupta, *J. Opt. A: Pure Appl. Opt.*, **9**, 555–559, 2007.
2. "Quasi-Gaussian output from dual Case I waveguide resonators with mirrors of step-index reflectivity profiles", J. Banerji, Subimal Deb, R. M. Jenkins, A. R. Davies. (Accepted in Applied Optics)
3. "Photonic crystal waveguide interferometer with  $\lambda/1000$  fringe spacing", Subimal Deb and J. Banerji (manuscript in progress)